



# Thermal Wave in Phonon Hydrodynamic Regime by Phonon Monte Carlo Simulations

Ben-Dian Nie and Bing-Yang Cao

Key Laboratory for Thermal Science and Power Engineering of Ministry of Education, Department of Engineering Mechanics, Tsinghua University, Beijing, China

## ABSTRACT

Thermal wave, namely wavelike behavior of heat propagation in transient heat conduction, enjoys much attention due to the recent investigations into phonon hydrodynamics in low-dimensional materials. In this paper, an improved phonon Monte Carlo (MC) simulation algorithm is developed based on the Callaway's dual relaxation time approximation model, which can deal with the coupling of normal and resistance scattering processes. Via the method, more thermal wave evidences are observed from the microscopic view of phonons, including overshooting and diffraction. Furthermore, the ballistic and hydrodynamic thermal waves are deeply studied. Two kinds of dissipation are found to exist in thermal waves, namely spatial dissipation and resistance dissipation. The former keeps the conservation of phonon momentum, but it lengthens the wavelength and decreases the peak temperature. The latter destroys the phonon momentum and keeps the original profile, lowering the peak temperature. Finally, phonon transport phenomena in Ziman hydrodynamic regime and diffusive regime are investigated, by introducing the scattering probability. The propagation tendency of thermal energy is found to decrease with the increasing scattering probability. The investigations into phonon hydrodynamics help to understand the heat transport characteristics and improve thermal management in low-dimensional materials.

## ARTICLE HISTORY

Received 16 February 2020  
Accepted 9 April 2020

## KEYWORDS

Thermal wave; second sound; phonon hydrodynamics; phonon Monte Carlo

## 1. Introduction

Thermal wave, or so-called heat wave, attracts much attention because of the fascinating wavelike behaviors of thermal transport [1–7], such as wave propagation [1–4], reflection [5–7], overshooting [8–10] and refraction [11–13]. The investigations originate from the failure of Fourier's law in infinite thermal perturbation speed and anomalous heat conduction [14–16] and anomalous heat conduction [17,18], and from the observation of the phenomena of second sound [19–26]. Several hyperbolic heat conduction models were introduced to describe the thermal waves [27–36], such as Cattaneo-Vernotte equation [25,26], phase lag model [27,28], Guyer-Krumhansl equation [29,30] and thermomass transport model [34–36]. All the above models admit the hyperbolic nature of heat transport. However, due to the lack of experimental evidences and even physical bases, they can just give phenomenological descriptions to thermal waves and the wave nature of heat requires further investigations.

The concept of phonons enables the microscopic image to understand heat transport phenomena from particle dynamics on the bases of Boltzmann transport equation [18, 37–51]. Tang et al. [43] adopted phonon Monte Carlo (MC) method to study the thermal wave and sorted them into two categories, namely ballistic thermal wave and hydrodynamic thermal wave. As for ballistic thermal

wave, phonons were free from being scattered and they propagated along with the original directions. And hydrodynamic thermal wave was dominated by normal scattering process (N process), where the phonon momentum was conserved. The transport behaviors of thermal waves in ballistic-diffusive regime were studied [39, 41–43] and it was found that the resistance scattering process (R process) dissipated the wave profiles exponentially. Recently, in low-dimensional materials [44,45], such as graphene and boron nitride a wide hydrodynamic window at a relatively high temperature were found, which drew much attention to the phonon hydrodynamics and hydrodynamic thermal waves [44–51]. Besides, the first experimental observations of second sound in graphite at temperature above 100 K demonstrated the transport behaviors of hydrodynamic thermal waves [52].

Numerical simulations are effective to obtain the propagation behaviors of thermal waves. Yao et al. [53] declared to observe the propagation of thermal waves in graphene based on molecular dynamics (MD). Cao and Tang [40–43] studied the thermal waves in ballistic-diffusive regime in nanofilms and nanowires and found the superballistic characteristics of ballistic thermal wave due to superposition. MC method can numerically solve the phonon Boltzman Transport Equation (PBTE) by tracing the life of phonons [54–63]. The previous MC algorithms focused more on the influence of R process and adopted Single Relaxation Time Approximation (SRTA) to solve the collision term [56–59]. Besides, some algorithms used the full scattering matrix [50,64], but they were limited to the investigations into the thermal conductivity in steady state due to the heavy calculation tasks. As Guyer defined [32,45], according to the scattering types, phonons are transported in different regimes, which are sorted into ballistic, Poiseuille hydrodynamic, Ziman hydrodynamic and kinetic (diffusive) regimes. Callaway [65] thought that R process and N process existed at the same time and N process had significant influences on thermal transport. Therefore, to include the effects of N process in transient heat transport, Lacroix *et al.* [54] assumed the directions of phonons were not altered after normal scattering process while R process emitted phonons in all directions evenly. Lee [63] proposed a method based on Dual Relaxation Time Approximation (DRTA), and adopted positive and negative energy particle couplings to conserve the thermal energy and phonon momentum. In this paper, an improved phonon MC algorithm is developed based on DRTA, which can consider the scattering mechanisms for N process by a complete probability function. One advantage of this algorithm is that the contributions of the two processes are separated clearly, which is helpful to deal with the coupled problems of R process and N process.

In Section 2, the details of the MC algorithm are presented. In Section 3, transient heat conduction processes are simulated to study the wave behaviors of phonons in hydrodynamic regime and a reasonable description of thermal waves from microscale viewpoint is obtained. Meanwhile, the difference between ballistic thermal wave and hydrodynamic thermal wave is discussed in detail. Furthermore, the transient heat transport phenomena in Ziman hydrodynamic regime and diffusive regime are investigated in Section 3.3.

## 2. Method

### 2.1. Phonon Monte Carlo algorithm

Monte Carlo method is an effective way to numerically solve the phonon Boltzmann transport equation. In this paper, the MC algorithm is developed to deal with the coupling of normal scattering process and resistance scattering process. The phonon Boltzmann equation,

$$\frac{\partial f(\mathbf{K}, \mathbf{x}, t)}{\partial t} + v_g(\mathbf{K}) \cdot \nabla f(\mathbf{K}, \mathbf{x}, t) = C f(\mathbf{K}, \mathbf{x}, t) \quad (1)$$

where  $\mathbf{K}$ ,  $x$ ,  $v_g$  are respectively the phonon vector, space coordinate and group velocity of phonons, describes the phonon propagation behaviors according to the drift process and scattering process.  $C$ ,

representing the phonon collisions, is very difficult to define exactly. Callaway's DRTA [65,66] model is adopted in this essay and the collision term is written as

$$Cf = \frac{f_0 - f}{\tau_R} + \frac{f_d - f}{\tau_N} \tag{2}$$

where  $f_0$  and  $f_d$  respectively represent the equilibrium Plank distribution

$$f_0 = \frac{1}{\exp(\frac{\hbar\omega}{k_B T}) - 1} \tag{3}$$

and displaced plank distribution

$$f_d = \frac{1}{\exp(\frac{\hbar\omega - \hbar\mathbf{K}\cdot\mathbf{u}}{k_B T}) - 1} \tag{4}$$

$\tau_R$  and  $\tau_N$  are the relaxation times of R process and N process, respectively.

It is assumed that the displaced Plank distribution  $f_d$  is the steady distribution of the phonon Poiseuille hydrodynamics.  $\mathbf{u}$  is the drift velocity of phonons, which is demonstrated to be independent from phonon vectors and phonon branches [44,51]. Thus, it is possible to describe the local thermal state with phonon density  $e(x)$  and drift velocity  $\mathbf{u}(x)$ . It lays the foundation of the following new algorithm.

The flowchart is plotted in Figure 1 to describe the phonon MC algorithm. First, phonons are emitted from the boundary with the given temperature. The drift process is discussed in Section 2.2. Since the whole system is divided into many cells, the cell energy and momentum are then recorded. The momentum here means that of the phonons being scattered in the normal scattering process in this time step. Afterward, the temperature  $T$  and drift velocity  $u_d$  are calculated, and they are important for

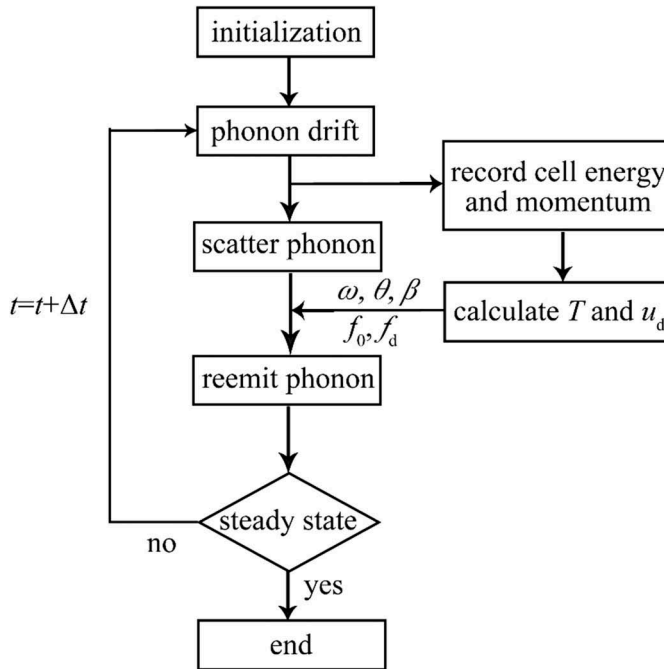


Figure 1. Flow chart of the phonon Monte Carlo algorithm.

the reemitting process. The scattering process is discussed in [Section 2.3](#). Finally, if the deviation of the system state with respect to the previous state is smaller than the threshold, which is set to be  $10^{-5}$  in the paper, it is thought that the system arrives at steady state, and the simulation is ended.

## 2.2. Phonon drift

Energy particles, rather than phonon particles, are adopted in the simulations to conserve the total thermal energy in a more precise way. If the total number of the energy particles keeps unchanged in the propagation process, the thermal energy is conserved. One energy particle is just a bunch of phonons with the same phonon vector and phonon branch, and the energy of each energy particle is the same. The energy particle transportation equation is obtained by multiplying  $\hbar\omega$  to Equation (1),

$$\frac{\partial e}{\partial t} + v_g \cdot \nabla e = \frac{e_0 - e}{\tau_R} + \frac{e_d - e}{\tau_N} \quad (5)$$

The control-variate variance-reduction method [59] is applied to reduce the calculation task. The reference energy density  $e_{\text{ref}}$  is chosen according to the circumstance. The phonon distribution of reference energy density is  $f_{\text{ref}}$  which is the equilibrium Plank distribution under temperature  $T_{\text{ref}}$ . The deviation energy density is defined as the difference between the local energy density and the reference one,

$$e^{\text{dev}}(x) = e(x) - e_{\text{ref}}(x) \quad (6)$$

Thus, the transportation equation is rewritten as

$$\frac{\partial e^{\text{dev}}}{\partial t} + v_g \cdot \nabla e^{\text{dev}} = \frac{e_0^{\text{dev}} - e^{\text{dev}}}{\tau_R} + \frac{e_d^{\text{dev}} - e^{\text{dev}}}{\tau_N} \quad (7)$$

In this way, the total number of energy particles can be reduced since only the deviation energy density is considered. The energy of each particles is

$$E_N = \frac{E}{N} \quad (8)$$

where  $E$  and  $N$  are, respectively, the total thermal energy and total number of the particle bunches emitted from the boundary per unit time. Since the phonon energy is determined by its frequency, the number of phonons in each bunch  $N_\omega$  is different,

$$N_\omega(\omega) = \frac{E_N}{\hbar\omega} \quad (9)$$

The frequency of each bunch is determined by

$$P_\omega(\omega) = \frac{\frac{1}{\exp(\frac{\hbar\omega}{k_B T}) - 1} - \frac{1}{\exp(\frac{\hbar\omega}{k_B T_{\text{ref}}}) - 1} \hbar\omega D(\omega)}{e - e_{\text{ref}}} \quad (10)$$

$D(\omega)$  is the phonon density of state and  $P_\omega$  is the probability density function for phonon frequency. The energy particles are transported in the medium before they are scattered. It is assumed that the distribution dissipates exponentially. Therefore, the free path of one single bunch is assumed to be

$$l = -l_{\text{MFP}} \ln R_l \quad (11)$$

where  $R_1$  is a random number produced by the system. The mean-free path  $l_{MFP}$  is derived from Matthiessen's rule,

$$l_{MFP}^{-1} = l_R^{-1} + l_N^{-1} \quad (12)$$

where  $l_R$  and  $l_N$  represent the mean-free paths of R process and N process, respectively.

Another significant problem is how to define temperature in the nonequilibrium state. Here, the classical method of determining the temperature value is adopted, which counts the total energy  $E_{\text{phonon}}$  in a unit volume. It is assumed that the temperature  $T_{\text{neq}}$  for  $E_{\text{phonon}}$  is equal to the temperature  $T_{\text{eq}}$  in the equilibrium state with the same thermal energy,

$$E_{\text{phonon}}(T_{\text{neq}}) = \int_K \int_V \frac{h\omega}{\exp(\frac{h\omega}{k_B T_{\text{eq}}}) - 1} d\mathbf{K} d\mathbf{r} \quad (13)$$

Temperature might be problematically defined in this way since the state is far away from equilibrium. This temperature is also called pseudo temperature in some studies [66]. Meanwhile, the phonons reemitted after scattering depend on the temperature, and the change of the definition for temperature will influence the results. Thus, it requires further investigations and discussion.

### 2.3. Phonon scattering

The phonons are scattered in two different ways, namely resistance scattering process and normal scattering process. R process leads to the equilibrium Plank distribution, while N process gives a tendency to the displaced Plank distribution. It is assumed that the phonons arrive at equilibrium state after being scattered, so that the frequency and velocity of the reemitted phonons follow the equilibrium Plank distribution or displaced Plank distribution. To describe the velocity vector in three-dimensional problems, two space angles are introduced, i.e., polar angle  $\theta$  and azimuth angle  $\beta$  as shown in Figure 2. The value of  $\theta$  varies in the range  $[0, \pi]$  while that of  $\beta$  varies in the range  $[0, 2\pi]$ .

The scattering type that one phonon undergoes is determined by the scattering probability  $M$ , which is defined as the portion of R scattering rates in total scatterings and calculated by the relaxation times,

$$M(\omega) = \frac{1/\tau_R(\omega)}{1/\tau_R(\omega) + 1/\tau_N(\omega)} \quad (14)$$

In the simulations, a random number  $R_M$  is obtained from the system and if  $R_M$  is smaller than  $M(\omega)$ , then resistance scattering process occurs and vice versa. One difference between R process and N process is that the velocity directions after R process are distributed evenly while N process has a preferential direction along with the drift velocity. The schematic diagram for these two scattering types has been plotted in Figure 3.

The DRTA method has been adopted, which assumes that phonons arrive at the steady state after one phonon-free path. When R scattering occurs, the frequency and velocity of reemitted phonons follow the equilibrium Plank distribution  $f_0$ ,

$$g_{R,\omega}(\omega) = \frac{\int_0^\omega h x (f_0 - f_{ref}) D(x) dx}{\int_0^{\omega_p} h x (f_0 - f_{ref}) D(x) dx} \quad (15)$$

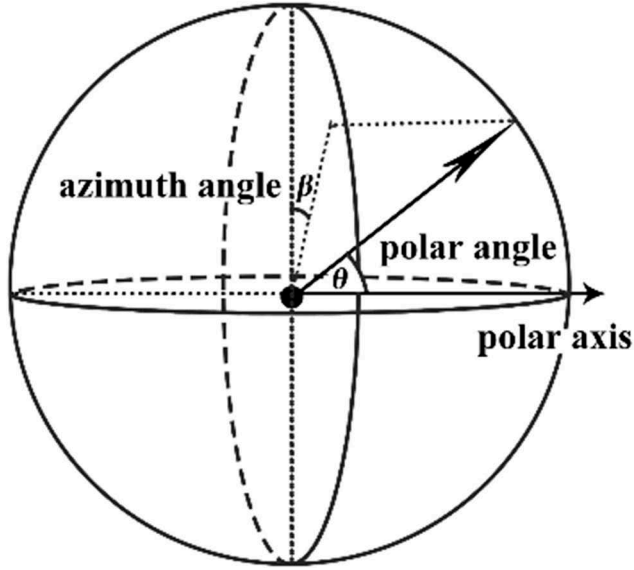


**Figure 2.** Schematic diagram for the phonon's space angles  $\theta$  and  $\beta$ .  $\theta$  is the polar angle from the polar axis, and  $\beta$  is the azimuth angle in the plane perpendicular to the polar axis.

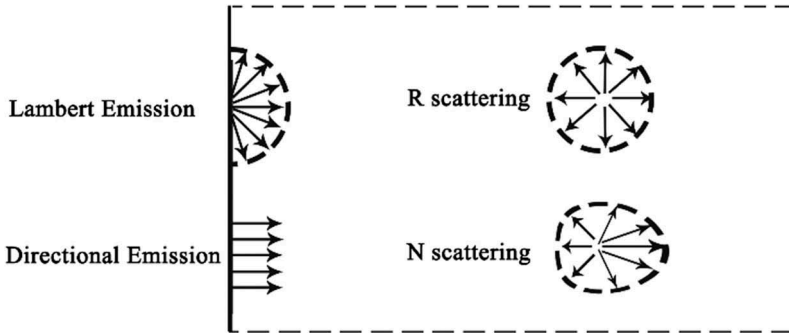


**Figure 3.** Schematic diagram for phonon resistance and normal scattering processes, and the Lambert emission boundary and directional emission boundary in MC simulations.

$$\omega = g_{R,\omega}^{-1}(R_\omega) \quad (16)$$

where  $R_\omega$  is the random number generated by the system. Equation (15) gives the probability distribution function of  $\omega$  and the inverse function Equation (16) gives the frequency based on  $R_\omega$ . In the simulations, this process is done by interpolations. Then  $\cos\theta$  is determined by

$$\cos\theta = 1 - 2R_\theta \quad (17)$$

and  $\beta$  is determined by

$$\beta = 2\pi R_\beta \quad (18)$$

$R_\theta$  and  $R_\beta$  are also the system random numbers. As for N process, it depends on the drift velocity  $\mathbf{u}_d$ . When the drift velocity  $\mathbf{u}_d$  is small, the displaced Plank distribution  $f_d$  can be dealt with in a linearized way,

$$f_d^{linear} = \frac{1}{\exp(\frac{\hbar\omega}{k_B T}) - 1} + \frac{\exp(\frac{\hbar\omega}{k_B T})}{(\exp(\frac{\hbar\omega}{k_B T}) - 1)^2} \frac{\hbar \mathbf{K} \cdot \mathbf{u}_d}{k_B T} = f_0 + f_0(1 + f_0) \frac{\hbar \mathbf{K} \cdot \mathbf{u}_d}{k_B T} \quad (19)$$

Due to the influence of drift velocity, the phonon directions are more concentrated. Therefore, the definition of drift velocity  $\mathbf{u}_d$  is important. Since the heat flux can be calculated in a statistical way,

$$\begin{aligned} \mathbf{q} &= \int_K \int_V f_d^{linear} \hbar \omega \mathbf{v}_g d\mathbf{K} d\mathbf{r} \\ &= \int_K \int_V \frac{\exp(\frac{\hbar\omega}{k_B T})}{(\exp(\frac{\hbar\omega}{k_B T}) - 1)^2} \frac{\hbar \mathbf{K} \cdot \mathbf{u}_d}{k_B T} \hbar \omega \mathbf{v}_g d\mathbf{K} d\mathbf{r} \end{aligned} \quad (20)$$

and  $\mathbf{u}_d$  is independent from phonon frequency [44], the relationship between the statistical heat flux  $\mathbf{q}$  and the drift velocity  $\mathbf{u}_d$  is derived,

$$\mathbf{u}_d = \mathbf{q}/p_D = \mathbf{q} / \int_K \int_V \frac{\exp(\frac{\hbar\omega}{k_B T})}{(\exp(\frac{\hbar\omega}{k_B T}) - 1)^2} \frac{\hbar \mathbf{K} \cdot \mathbf{q}}{k_B T} \hbar \omega \mathbf{v}_g d\mathbf{K} d\mathbf{r} \quad (21)$$

where  $p_D$  is adopted to just simplify the expression, and  $|\mathbf{q}|$  is the norm of heat flux  $\mathbf{q}$ . In this way, the scalar  $p_D$  is an integration that is determined by temperature and cutoff frequency. The interpolation matrix is calculated at the beginning which contains different values of  $p_D$  at different temperatures to reduce the calculation tasks. During one time step, the phonon particles could be scattered or propagate along the original path. In this algorithm, the drift velocity is supposed to be determined by those phonons that have been scattered in the scattering process, instead of all the phonons in the area. So here  $\mathbf{u}_N$  is used to represent the drift velocity of the phonons being scattered instead of  $\mathbf{u}_d$ . The heat flux  $\mathbf{q}_N$  is counted as

$$\mathbf{q}_N = \sum_i^{N_{scattering}} E_N \mathbf{v}_g \quad (22)$$

where  $N_{scattering}$  is the total number of phonons that are scattered in this time step. When N process is coupled with R process, the heat flux is supposed to be the heat flux produced the phonons scattered by normal scattering process. Then, the drift velocity  $\mathbf{u}_N$  is calculated as

$$\mathbf{u}_N = \frac{\mathbf{q}_N}{p_D} \quad (23)$$

Nevertheless, it is not proper to use this drift velocity  $\mathbf{u}_N$  directly in the probability density function, because the heat flux  $\mathbf{q}_N$  only includes the contributions of those phonons that are scattered while  $p_D$  considers the influences of all the phonons in the area. Therefore, a revised drift velocity  $\mathbf{u}_{dr}$  is introduced to make the correction,

$$\mathbf{u}_{dr} = \mathbf{u}_N \cdot \frac{E_{total}}{E_{scattering}} \quad (24)$$

$E_{total}$  is the total energy in the designated regime while  $E_{scattering}$  is the energy of phonons which are scattered in the normal scattering way. It can be demonstrated that by adopting  $\mathbf{u}_{dr}$  as  $\mathbf{u}_d$  in Equation (19), this algorithm conserves the phonon momentum after the scattering process. At the same time,

in steady state  $\mathbf{u}_{dr}$  becomes the same to  $\mathbf{u}_d$ , which is the drift velocity of all the phonons in this area. The temperature  $T$  and drift velocity  $\mathbf{u}_d$  determine the reemitting process of phonons after normal scattering process.

The phonon frequency after N process is determined by the following expression,

$$g_{N,\omega}(\omega) = \frac{\int_0^\omega \hbar x (f_d^{linear} - f_{ref}) D(x) dx}{\int_0^{\omega_D} \hbar x (f_d^{linear} - f_{ref}) D(x) dx} \quad (25)$$

$$\omega = g_{N,\omega}^{-1}(R_\omega) \quad (26)$$

As for the space angle, since the drift velocity is a vector, the polar axis can be taken along with the direction of the drift velocity  $\mathbf{u}_d$ . Thus, the scattering directions of phonons can be obtained in the relative coordinate. Then, the rotation matrix can be adopted to rotate the coordinate to the absolute coordinate, where the phonons propagate in real space. Considering the linearized displaced Plank distribution (Equation (19)), the probability function for polar angle  $\theta$  is

$$g_{N,\theta}(\theta) = \frac{\int_0^\theta [p_1 + p_2 u_d \cos \theta_1] \hbar \omega \sin \theta_1 D(\omega) d\theta_1}{P_0} \quad (27)$$

$$\theta = g_{N,\theta}^{-1}(R_\theta) \quad (28)$$

where

$$p_1 = f_0 - f_{ref} \quad (29)$$

$$p_2 = f_0(1 + f_0) \frac{\hbar K}{k_B T} \quad (30)$$

$$P_0 = \int_0^\pi \left[ f_0 - f_{ref} + f_0(1 + f_0) \frac{\hbar K u_d}{k_B T} \cos \theta_1 \right] \hbar \omega \sin \theta_1 d\theta_1 \quad (31)$$

and  $g_{N,\theta}$  is called the probability distribution function while

$$f_{N,\theta}(\theta, \omega) = [p_1 + p_2 u_d \cos \theta] \hbar \omega \sin \theta D(\omega) / P_0 \quad (32)$$

is called the probability density function. The azimuth angle  $\beta$  is distributed evenly so that

$$\beta = 2\pi R_\beta \quad (33)$$

One problem occurs when the drift velocity is not small enough so that

$$|f_0 - f_{ref}| < \left| f_0(1 + f_0) \frac{\hbar |\mathbf{K}| \cdot |\mathbf{u}_d|}{k_B T} \right| \quad (34)$$

The probability could be negative when the space angle  $\theta$  is larger than the critical one,

$$\cos \theta_{\text{critical}} = \frac{f_0 - f_{\text{ref}}}{f_0(1 + f_0) \frac{\hbar |\mathbf{K}| \cdot \mathbf{u}_d}{k_B T}} \quad (35)$$

So Equation (32) is incorrect for the negative probability case. Thinking about that  $f_0$  might be smaller than  $f_{\text{ref}}$ , there are two different density distributions, as shown in Figure 4. It is found that the probability density function and distribution function can be divided into three parts in both the two conditions. When  $p_1 > 0$ , in Figure 4a, the integration of part 1 in density function equals 1. The probability density in part 2 is positive while that in part 3 is negative. The integration of probability densities of part 2 and part 3 is 0, so that the total distribution function comes to 1 in the end as shown in Figure 4b. When  $p_1 < 0$  which means the steady temperature  $T$  is lower than the temperature of circumstance  $T_{\text{ref}}$  in order to guarantee the total integration positive, a minus sign must be added to the probability density function. Then, the following conditions are satisfied:  $p_1 > 0, p_2 < 0$ . As shown in Figure 4c,d, part 1 is negative while part 2 is positive, and the integration of these two parts is equal to 0. Then, the integration increases monotonously to 1 in part 3. The negative probability density is unphysical but it is reasonable in mathematical meaning. If only part 1 in Figure 4a and part 3 in Figure 4c are taken into consideration, the phonon momentum cannot be conserved. It means that new energy particles are born after scattering besides the original ones. Here the angle of zero limit  $\theta_{\text{zero}}$  is introduced, which satisfies the following equation:

$$\int_0^{\theta_{\text{zero}}} [p_1 + p_2 u_d \cos \theta_1] \hbar \omega \sin \theta_1 D(\omega) d\theta_1 = \begin{cases} P_0 & p_1 > 0 \\ 0 & p_1 < 0 \end{cases} \quad (36)$$

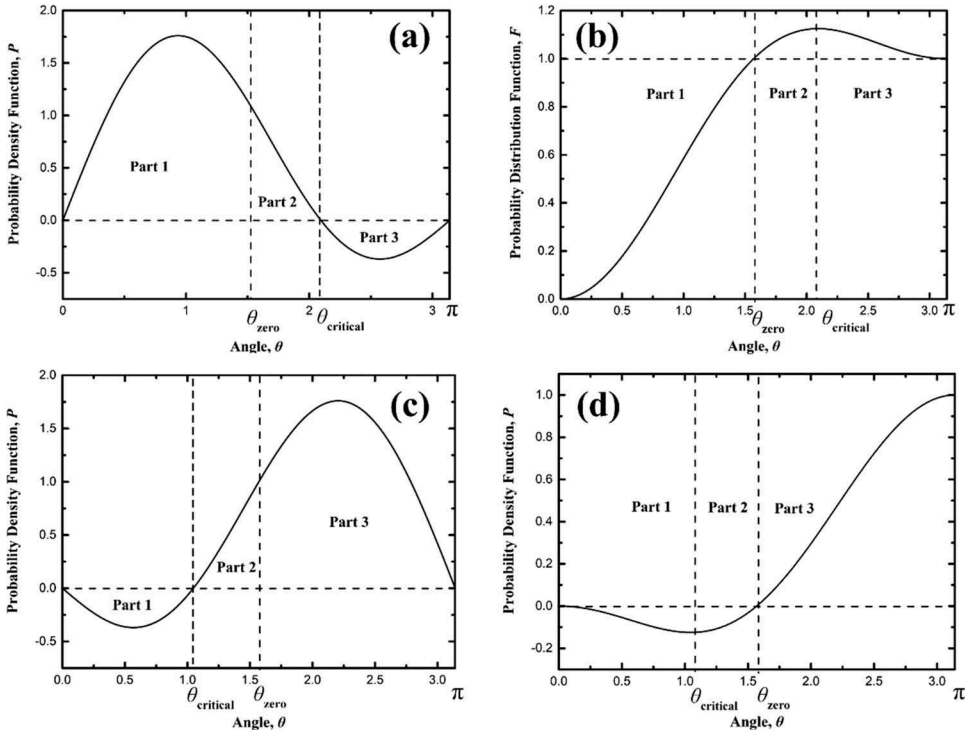


Figure 4. Probability density function  $f_{N,\theta}$  and probability distribution function  $g_{N,\theta}$  of the two different linearized displaced Plank distribution when Equation (33) holds. (a) is the probability density function and (b) is the probability distribution function when  $p_1 > 0$  while (c) and (d) are the probability density function and probability distribution function for  $p_1 < 0$ , respectively.

The sum of the accumulated probability from 0 to  $\theta_{\text{zero}}$  is equal to 1 or 0. Therefore,  $\theta_{\text{zero}}$  is the boundary of part 1 and part 2 in Figure 4a and the boundary of part 2 and part 3 in Figure 4c.

Peraud [59] adopted negative energy particles as he introduced the control-variance variate-reduction method in MC simulations. The reemitting particles at the same location and time step had the same sign, determined by the deviation of local energy density with respect to the reference one, free from phonon frequency. Lee [63] adopted particle pairs to conserve the phonon momentum with the conservation of thermal energy in the normal scattering process. The signs of particle energy were determined by the wave vectors  $\mathbf{q}_x$  and temperature gradient direction  $\nabla T$ , where positive energy particles were drawn at  $q_x > 0$  and negative ones appeared when  $q_x < 0$ . In this paper, the energy particle pairs are further developed, where the signs are related to phonon frequency and phonon wave vector. In one pair, two particles have the same amount of energy with, however, different signs. If the number of the negative energy particles is regarded to be minus, the total particle number keeps the same because the same quantities of positive energy particles and negative energy particles are born. Thus, the thermal energy is conserved strictly. For example, in Figure 4a, the original energy particles, positive energy particles, and negative energy particles correspond to part 1, part 2, and part 3, respectively. And the number of new energy particle pairs is determined by the ratio of integration of part 2  $I_2$  with respect to the integration of part 1  $I_1$ . Meanwhile, the integration  $I_2$  is equal to minus  $I_3$ ,

$$I_2 = -I_3 > 0 \quad (37)$$

$$\frac{I_2}{I_1} = n_{\text{new}} + r_{\text{new}} \quad (38)$$

where  $n_{\text{new}}$  and  $r_{\text{new}}$  are the integer part and decimal part of the ratio, respectively. If  $n_{\text{new}} \geq 1$ , then  $n_{\text{new}}$  pairs of new phonon bunches are emitted. A random number  $r_{\text{rand}}$  is generated by computer. If  $r_{\text{rand}} < r_{\text{new}}$ , then one new pair of phonon bunches is emitted. Otherwise, no new bunch is born. The concept of negative energy particles might be confusing at first sight. Consider that the deviation distribution is established on the foundation of a reference distribution  $f_{\text{ref}}$  and the negative sign only means that the local energy density is lower than the reference one. Thus, it does not mean that the absolute thermal energy is lower than 0. In this way, the negative energy particles can be seen as energy holes, corresponding to positive electrons. The energy holes propagate in the opposite direction of the energy flux. In the scope of this paper, the behaviors of negative energy particles and energy holes are demonstrated to be the same, which is shown in the following section. However, they are not totally the same in the case when the reference state is near absolute zero temperature. By introducing negative and positive energy particle pairs in the MC algorithm, the phonon momentum can be conserved in a statistical view according to the complete probability function while the total thermal energy keeps conserved strictly. When the phonon number is large, the difference between the momentums before and after scattering can be ignored.

As it is mentioned before, the rotation matrix is adopted since the drift velocity  $\mathbf{u}_{\text{dr}}$  introduces the spatial structure. The space angles of  $\mathbf{u}_{\text{dr}}$  are  $\theta_{\text{dr}}$  and  $\beta_{\text{dr}}$ ,

$$\mathbf{u}_{\text{dr}} = (u_{\text{dr}} \cos \theta_{\text{dr}}, u_{\text{dr}} \sin \theta_{\text{dr}} \cos \beta_{\text{dr}}, u_{\text{dr}} \sin \theta_{\text{dr}} \sin \beta_{\text{dr}})^{\text{T}} \quad (39)$$

Therefore, for a wave vector  $\mathbf{K}$  which is defined based on  $\mathbf{u}_{\text{dr}}$ ,

$$\mathbf{K} = (K \cos \theta, K \sin \theta \cos \beta, K \sin \theta \sin \beta)^{\text{T}} \quad (40)$$

the rotation matrix can be written as

$$\mathbf{M}_{rotation} = \begin{bmatrix} \cos \theta_{dr} & 0 & -\sin \theta_{dr} \\ \sin \theta_{dr} \cos \beta_{dr} & \sin \beta_{dr} & \cos \theta_{dr} \cos \beta_{dr} \\ \sin \theta_{dr} \sin \beta_{dr} & \cos \beta_{dr} & \cos \theta_{dr} \sin \beta_{dr} \end{bmatrix} \quad (41)$$

and the wave vector in the original coordinate  $\mathbf{K}^*$  is

$$\mathbf{K}^* = \mathbf{M}_{rotation} \mathbf{K} \quad (42)$$

## 2.4. Boundary conditions

When phonons interact with a boundary, they are scattered in different ways according to different boundary conditions. Based on the heat flux going across the boundary, isothermal boundary and adiabatic boundary can be defined. The isothermal boundary emits the phonons into the regime according to the boundary temperature and the phonons arriving at the boundary are absorbed totally. The adiabatic boundary does not emit any phonons itself. Instead, it reflects back all the phonons arriving at the boundary. When the phonons are reflected back, the rough boundary and smooth boundary take effects. When the boundary is totally rough, the momentum of the arriving phonons is totally destroyed and the phonons are reemitted randomly. When the boundary is totally smooth, the phonon momentum parallel with the boundary is conserved while that perpendicular to the boundary is inverted back. Here, it is assumed that the frequency of reemitting phonons follows equilibrium Plank distribution under the boundary temperature.

The temperature boundary conditions and heat flux boundary conditions are defined in this paper as follows. As the temperature boundary condition can be seen as the contact interface of two media with different temperature, the phonons emitting from the boundary follow the Lambert distribution,

$$P(\theta) = I_0 \cos \theta \quad (43)$$

Heat flux is a vector with length and direction. If a heat flux boundary condition is defined as

$$\begin{cases} q_x(x=0, y, z) = q_0 \\ q_y(x=0, y, z) = 0 \\ q_z(x=0, y, z) = 0 \end{cases} \quad (44)$$

the directions of phonons are supposed to go along the direction of heat flux. In this paper, the directional boundary is adopted to represent the heat flux boundary, where all the phonons have the same direction to the heat flow. As for the boundary condition in Equation (44), the angle distribution is

$$P(\theta) = \delta(\theta) \quad (45)$$

and there are no other directions except the one along with  $x$  coordinate. The schematic diagrams of Lambert emission and directional emission are plotted in [Figure 2](#). Generally speaking, the heat flux boundary can be regarded as the combination of directional emission and Lambert emission while the ratio of these two kinds of distribution is determined by the state of the boundary and heating ways, such as boundary roughness and laser heating.

## 2.5. Simulation details and verification

The total number of energy particles taken in this paper is  $2 \times 10^7$ , and the time step is 0.01 ps. The regime is set to be 500 nm×200 nm×100 nm, and smooth boundary conditions are adopted in  $y$  and  $z$  directions. If there is no specific illustration, the reference temperature is 100 K and the boundary

temperature is set to be 101 K. The Debye temperature is 1200 K. The isothermal boundary condition which emits and absorbs phonons based on constant temperature boundary is used. In this paper, only one phonon branch is taken into consideration. Debye model is used which assumes a linearized relationship between the phonon frequency and the phonon wave vector,

$$\omega = v_g K \quad (46)$$

where  $v_g$  is the phonon group velocity, and the cutoff frequency is determined by the Debye temperature. To make the principles clearer, gray model is adopted and the influences of phonon frequency on relaxation times are ignored. The relaxation time of N process is assumed to be 10 ps. Since the group velocity of phonons is 5000 m/s, the mean-free path of N process is 50 nm.

To verify this MC algorithm, the simulations results are compared with the previous results of semi-analytic solutions [50] and another MC method proposed by Lee [63]. The results show the effect of width with coarse boundary in phonon hydrodynamics regime. The phonon group velocity is  $10^4$  m/s, and scattering rate for normal scattering process is  $10^{10} \text{ s}^{-1}$ . The Debye temperature is set to be 1200 K and the material temperature is 100 K as in reference [63]. The results in Figure 5 validate the current algorithm.

Besides, the influences of adopting negative energy particles instead of energy holes are analyzed. Here, an initial value problem is simulated to compare these two methods. The calculation system details are as follows. As for negative energy particles, the initial energy density distribution is set to be,

$$density(x) = E_0 + \begin{cases} -\Delta E & 2 < x/D < 3 \\ 0 & x < 2 \text{ or } x > 3 \end{cases} \quad (47)$$

And as for energy hole, the initial energy distribution is,

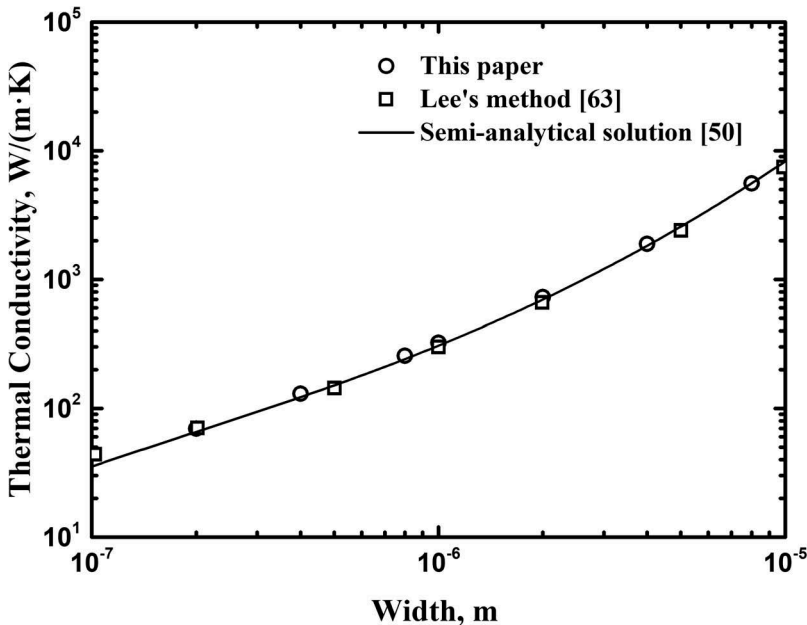


Figure 5. Comparisons of the predictions for width-dependent thermal conductivity between the current algorithm and other researches.

$$density(x) = E_0 + \begin{cases} 0 & 2 < x/D < 3 \\ \Delta E & x < 2 \text{ or } x > 3. \end{cases} \quad (48)$$

And in both the cases, the initial heat flux is zero. Figure 6a depicts the propagation profiles with energy holes while Figure 6b depicts those with negative energy particles. These two methods lead to the same time evolution profiles. This verification demonstrates that it is reasonable to introduce the energy particles with negative energy in the simulations.

Lee [63] adopted a similar algorithm to simulate the momentum-conserved process by dividing the probability function into two parts, which makes sure the energy before and after the process are the same first and arrives at momentum conservation by adding and deleting phonons. The algorithm in this paper uses the complete probability function to reemit phonons after scattering. It can reduce the amount of phonons simulated in the process because the negative probability and positive probability reduce each other via summing up. However, it also leads to the negative probability problem, which is solved in this paper by positive and negative energy particle pairs. More advantages are that this algorithm divides the contributions of normal scattering process and resistance scattering process and that the introduction of the concept for phonon drift velocity makes the simulations of N process clearer. Meanwhile, although the equality of energy holes and negative energy particles has been widely used in steady heat transfer, the application in transient heat conduction problems is testified in this paper to make sure the simulations feasible. Meanwhile, although the equality of energy holes and negative energy particles has been widely used in steady heat transfer, the application in transient heat conduction problems is testified in this paper to make sure that the simulations are right.

### 3. Results and discussion

#### 3.1. Characteristics of thermal waves

The non-Fourier models predict the wavelike behaviors of heat by introducing the derivative of heat flux with respect to time. Experimental observations of the finite speed and the phase inversion of second sound support the predictions of hyperbolic heat conduction equations. However, even though it is declared that the second sound can be observed in two-dimensional materials, it is still far away to measure the transient temperature change in such small length and interval to provide more wavelike behavior evidences in experiments. Therefore, this section intends to observe the wave behaviors from the microscopic level based on phonon MC simulations. All the simulations in this section are set in the phonon hydrodynamic regime, where N process dominates and R process is omitted.

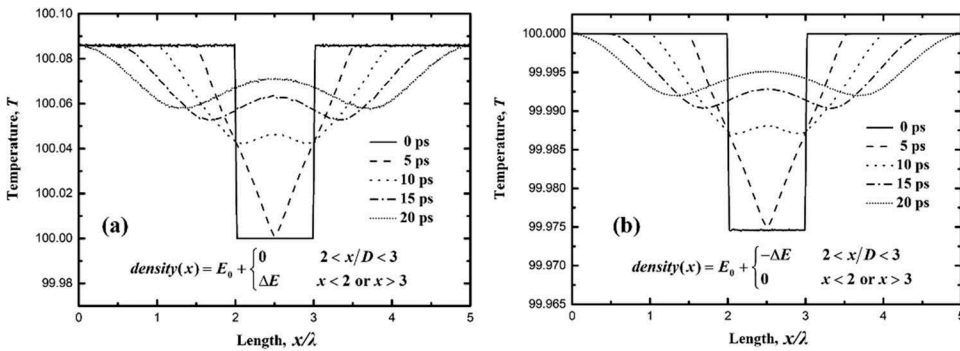


Figure 6. Energy distribution patterns along with time when the energy holes (a) and the negative energy particles (b) are adopted with the initial condition (47) or (48).

### 3.1.1. Overshooting

Overshooting phenomenon occurs during the superposition of thermal waves, and it has been predicted by various non-Fourier models [8–10, 43]. On the one hand, overshooting reveals the failure of classical Fourier's law because a higher temperature peak appears in the combined wave than the original waves. On the other hand, it also leads to the discussion of unsteady temperature. In this case, local thermal equilibrium assumption does not hold and the definition of temperature fails. In some sense, the temperature here is more like the measurement of local phonon energy density.

Overshooting usually occurs when a thermal wave is reflected back by boundary or two thermal waves in opposite directions meet with each other [8], as shown in Figure 7. As for the reflection, when the reflection wave meets with the incident wave, a higher temperature appears. In the following case,  $\lambda$  is the phonon mean free path and the length of the regime is  $10\lambda$ . The initial temperature is the room temperature, 300 K and Debye temperature is 1200 K. All the boundaries are set to be smooth and adiabatic, so that the thermal wave can be reflected back. At the beginning, a heat pulse is applied to the left boundary and a thermal wave comes into being and propagates toward right (Figure 7a). The temperature distribution of the incidence wave is plotted at time  $t = 40$  ps, displayed in Figure 8. Then, when time comes to 50 ps, the thermal wave arrives at the boundary as shown by the dash line and some phonons are reflected back. It is difficult to tell the incidence wave and reflection wave individually, but the result of higher temperature peak value at time  $t = 60$  ps implies the combination of these two waves. After that, the reflected thermal wave continues propagating toward the left as depicted at  $t = 90$  ps and 100 ps.

Another case happens when two thermal waves propagating in opposite directions meet with each other. A plate with finite length is considered. Two heat pulses are applied at both boundaries of the plate, producing two thermal waves in opposite directions, as shown in Figure 7b. Figure 9a describes the temperature distribution patterns along with time when only the left boundary is heated by the heat pulse. It is used to compare with Figure 9b where both sides are heated, to investigate the propagation behaviors of the thermal waves. In Figure 9b, the solid black line depicts the temperature distribution of these two thermal waves at  $t = 10$  ps. At  $t = 20$  ps, these two waves keep dissipating in the propagation process and meet with each other for the first time. Then, the meeting behaviors of these two waves occur at  $t = 30$  ps and 40 ps. It can be observed that the peak temperature value at time  $t = 30$  ps is higher than that at time  $t = 20$  ps, demonstrating the existence of overshooting when two groups of phonons meet. After that, the two waves separate and keep their original directions. The propagation patterns of an individual thermal wave from the left boundary are plotted in Figure 9a to analyze the influences of overshooting, where a single wave propagates forward with time going on. When the distribution patterns at time  $t = 40$  ps and 50 ps in Figure 9b are compared with those in Figure 9a, it can be seen that after separation, the wave keeps its original shape and direction, free of the influence of the other wave. It obeys the rules of wave superposition. The above behaviors are just like the behaviors of

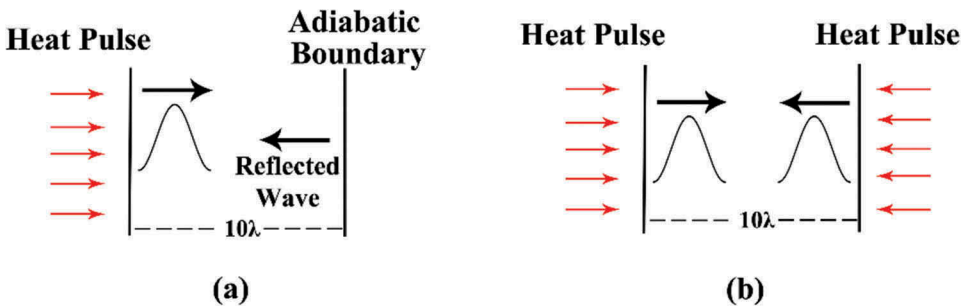


**Figure 7.** Schematic diagrams of the simulation models. (a) A thermal wave is reflected back by the adiabatic boundary. (b) Two thermal waves propagating in opposite directions meet with each other.

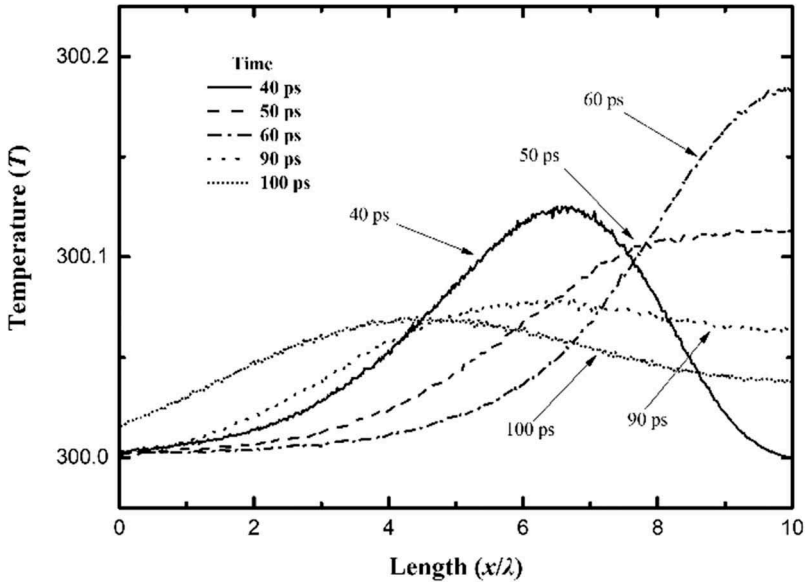


**Figure 8.** Temperature profiles along with time at  $t = 40, 50, 60, 90,$  and  $100$  ps when a thermal wave meets an adiabatic boundary and then moves back.

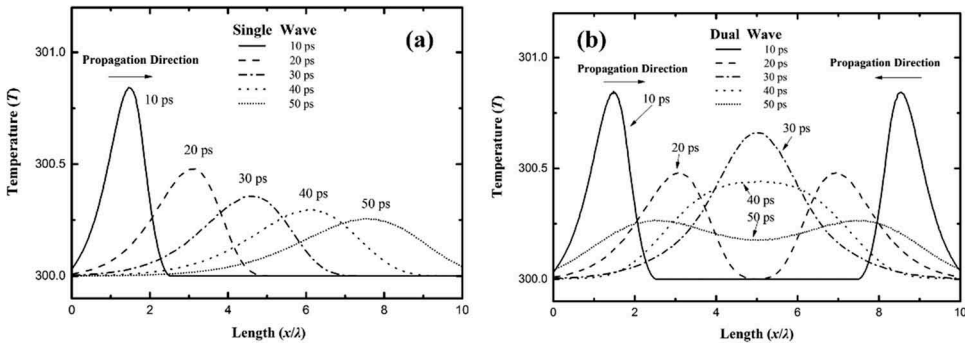


**Figure 9.** Temperature profiles along with time at  $t = 10, 20, 30, 40,$  and  $50$  ps for the situations: (a) A single thermal wave propagates from the left to the right; (b) Two thermal waves from different boundaries meet with each other in opposite directions.

mechanical waves. However, the difference is that these waves are produced by groups of phonons, which are regarded as individual particles in solid physics. It is interesting to observe the wave behaviors presented by particles.

### 3.1.2. Diffraction

Diffraction and refraction are thought to be symbols of waves [11–13]. For example, water ripples change their directions when there is an obstacle or a hole in the path, and spread again with the obstacle as the new wave source. In this section, the diffraction phenomenon of thermal wave has been observed in a two-dimensional regime.

In order to simulate the diffraction phenomenon, a square plate with finite width and length is considered as shown in Figure 10. The initial temperature is 100 K. The length and width of the plate are equal and set to be 1, and the phonon mean free path is 0.2.  $x$  and  $y$  coordinates represent the length and width, respectively. There is an adiabatic wall parallel with  $y$  coordinate, namely along the

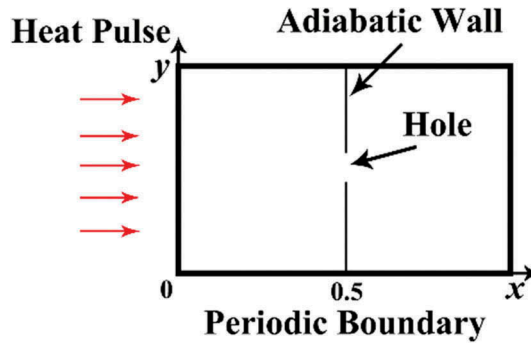


Figure 10. Schematic diagram for the diffraction simulation models.

direction of width at  $x = 0.5$ . A hole appears in the wall from  $y = 0.48$  to  $y = 0.52$ , which is smaller than the wavelength of thermal wave, allowing phonons to get across the wall. As for thermal wave, the wavelength becomes larger during the propagation. It is difficult to give a standard wavelength, and the appearance wavelength represents the heat pulse duration, rather than the conventional wavelength. Therefore, the hole is set to be as small as it can. At the beginning, the left boundary is heated by heat pulse to produce a thermal wave. The temperature distribution in the plate at time  $t = 15$  ps, 30 ps, and 50 ps is depicted in Figure 11, represented by the heights of the profiles.

The temperature distribution in the whole plate is displayed in Figure 11A.1-A.3 with the color map Legend 1. Considering that the thermal energy getting through the hole is much less than the thermal energy in the left, the figures of the temperature distributions in the right regime are magnified specifically in Figure 11B.1-B.3 where the color map obeys Legend 2. Figure 11A.1 shows the propagation patterns of thermal wave before it meets the hole. At time  $t = 30$  ps, the thermal wave arrives at the wall and some phonons have already passed through the hole. There are ripples spreading in the right regime. Figure 11B.2-B.3 has clearer distribution patterns for the ripples. It is very interesting to find the phase inversion in Figure 11(A.3) and 11(B.3). The hole in the wall has already become the new wave source and produces thermal perturbation. Meanwhile, the reflection wave appears, which propagates toward the left after meeting the wall.

In the above simulations, the phenomena of overshooting and diffraction have been observed, which are regarded as the wave characteristics. Although the heat transport is determined by the phonons in dielectric solids which are regarded as particles, the transient processes own the wavelike behaviors due to the activities of phonon groups. More wave characteristics of thermal waves can be observed in the phonon level based on this MC algorithm.

### 3.2. Thermal wave and hyperbolic models

The wavelike behaviors of heat in crystals are demonstrated to originate from phonon momentum conservation [43]. N process can keep the phonon momentum in the collision processes. Nevertheless, there is another kind of heat transport phenomenon where phonon momentum is conserved, i.e., ballistic heat transport. Therefore, the wavelike behaviors can be sorted into two categories based on the scattering mechanism, namely hydrodynamic thermal wave [44,45] and ballistic thermal wave [40–43].

#### 3.2.1. Ballistic and hydrodynamic thermal waves

Even though thermal waves are sorted into two categories, these two waves always exist at the same time in heat conduction problems. Thermal waves induced by temperature boundary and heat flux

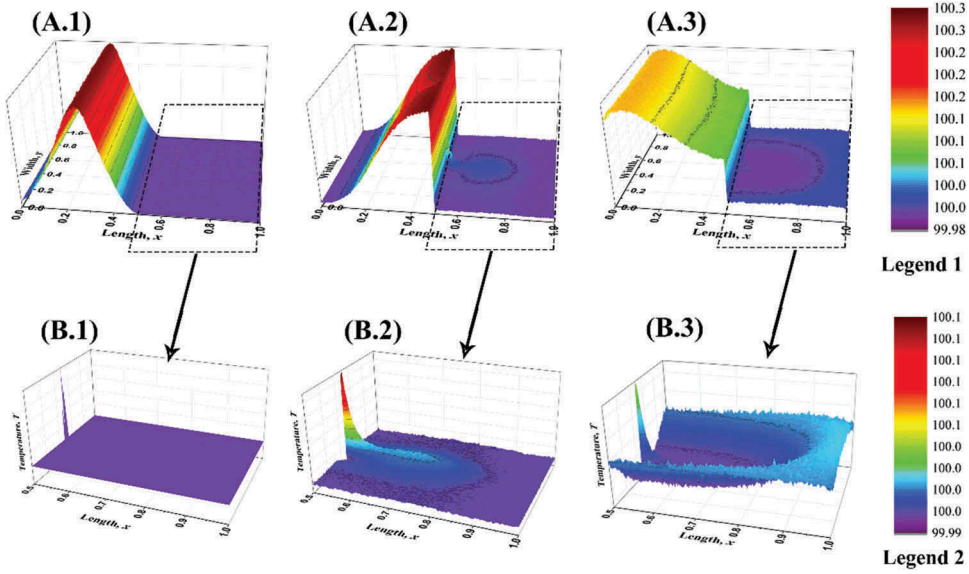


**Figure 11.** Temperature distribution patterns for the diffraction phenomena of thermal waves when they pass through a hole in the adiabatic wall at time  $t = 15, 30,$  and  $50$  ps. The heights and colors of the profiles denote the different values based on the color map legend 1 on the right. (B.1-B.3) are the magnified figures based on Legend 2 for the right zone.

boundary are analyzed below. A one-dimensional heat conduction problem is considered, which can be seen as a plate with finite length and infinite width and height. The initial temperature is 300 K and Debye temperature is 1200 K. A sine-shape heat pulse is applied to the left boundary,

$$q = \begin{cases} A_1(1 - \cos(2\pi t/t_0)) & t < t_0 \\ 0 & t > t_0 \end{cases} \quad (49)$$

as is shown in Figure 12.  $t_0$  is equal to 10 ps and  $A_1$  is a constant coefficient. A single thermal wave is produced from the left boundary and its propagation patterns are shown in Figure 13.

Figure 13a–c shows the temperature profiles, energy density profiles and drift velocity ratio distribution in the temperature boundary at different times  $t = 10, 25, 50, 75,$  and  $100$  ps, and Figure 13d–f show these patterns under the heat flux boundary. The drift velocity ratio is the ratio of the drift velocity  $\mathbf{u}_d$  with respect to the phonon velocity  $\mathbf{v}_g$ ,

$$r = \frac{\mathbf{u}_d}{\mathbf{v}_g} \quad (50)$$

The propagation of thermal waves describes the transport process of thermal energy and this process can be presented by temperature distribution, energy density distribution, or heat flux distribution. In this paper, to make it easier to understand, the temperature field is adopted to depict the thermal wave propagation. The differences of these two boundary conditions have already been discussed in Section 2.4. In the simulations, R process is ignored and all the collisions are momentum-conserved. As for the temperature boundary, phonons are emitted from the left boundary according to the Lambert distribution. The energy density distribution in Figure 13b,e is normalized by the peak value at time  $t = 10$  ps. It can be seen that temperature wave profiles come into being at  $t = 10$  ps, and then the profiles propagates forward. During that process, the peak value of the temperature profile decreases and the wavelength becomes larger. It means that the thermal wave has been dissipated. It is very interesting to discuss the dissipation in phonon hydrodynamic regime, because

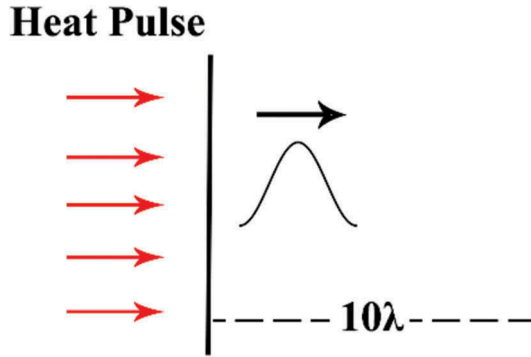


**Figure 12.** Sketch diagram for the one-dimensional heat conduction problem where the left boundary is heated by a sine-shape heat pulse to produce a single thermal wave.

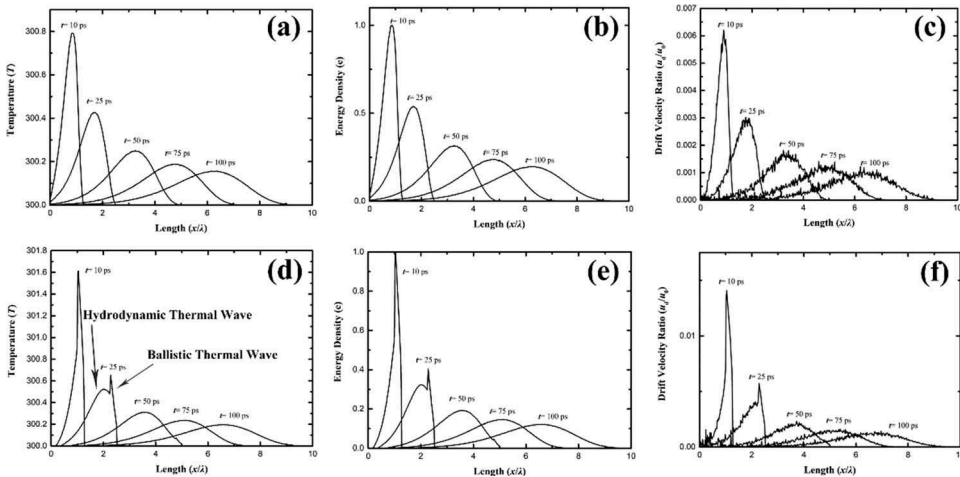


**Figure 13.** Propagation patterns of hydrodynamic thermal waves represented by temperature, normalized energy density, and drift velocity ratio. (a-c), with temperature boundary condition following Lambert distribution, are the temperature patterns (a), energy density patterns (b), and drift velocity ratio patterns (c). (d-f) with heat flux boundary condition following directional distribution, are the temperature distribution (d), energy density distribution (e) and drift velocity ratio distribution (f), respectively.

there is no resistance in the propagation and collision processes and dissipation is not supposed to appear as well. However, the peak value of the wave profiles does become lower. This kind of dissipation comes actually from the spatial direction dispersion. The phonons have different directions in space although they have the same drift velocity. Faster phonons go further and the distance between the front and the end of the wave becomes larger and larger, leading to the dissipation of thermal waves. This kind of dissipation is called spatial dissipation in this paper, different from the resistance dissipation induced by R process, where the phonon momentum is seriously destroyed.

The speed direction dispersion has been widely investigated. Phonon Boltzmann equation indicated the convective effect of phonon momentum, which shows the spatial distribution of phonon velocity directions [65]. Guyer and Krumhansl [31,32] added the viscosity term and gradient term to the macroscale heat conduction equation based on linearized phonon Boltzmann equation to describe the effects of boundary and spatial dispersion. Hardy [67] defined the velocity of second sound considering the phonon velocity in real space. Recently, Tang [41] discussed the spatial dissipation in ballistic thermal

waves. As for normal scattering process, Lee [63] investigated the thermal resistance caused by the transition from non-collective distribution to collective distribution in the view of entropy production. He demonstrated that there is no entropy production in phonon hydrodynamics when there is no spatial dispersion. Here, we study the spatial dissipation in transient heat conduction.

In Figure 13c, it is found that the drift velocity ratio profile propagates along with the propagation of temperature profile, and the peak of the temperature profile has higher drift velocity. The phonons do not have a unified drift velocity in transient heat transport. In fact, according to the definition of drift velocity, the drift velocity profiles reveal the distribution of heat flux in the numerical regime. The transport of thermal wave is also the transport of heat flux, as mentioned before. In Figure 13d–f, the directional heat flux boundary is considered. The ballistic phonons produce a sharp front of wave at time  $t = 10$  ps as shown in Figure 13d. As the phonons are scattered with time going on, the thermal wave comes to the hydrodynamic type. At  $t = 25$  ps, a coupled wave shape by ballistic thermal wave and hydrodynamic thermal wave is displayed. The sharp front belongs to the ballistic part and the gentle tail is caused by the hydrodynamic part. Since most of the ballistic phonons have already been scattered at time  $t = 50$  ps, the final profile patterns of Figure 13a,d become the same, implying a completely hydrodynamic thermal wave.

Before discussing the difference between hydrodynamic and ballistic thermal waves, some numerical experiments are conducted. The directional heat flux boundary is adopted and two different heat pulse types are applied, namely the rectangular type and triangular type, as shown in Figure 14. As for the rectangular heat pulse, the heat flux boundary is taken as

$$q(x = 0, t) = \begin{cases} A_2 & t \leq t_0 \\ 0 & t > t_0 \end{cases} \quad (51)$$

And the triangular heat pulse is

$$q(x = 0, t) = \begin{cases} A_2 \frac{2t}{t_0} & t \leq \frac{t_0}{2} \\ A_2 (2 - \frac{2t}{t_0}) & \frac{t_0}{2} < t \leq t_0 \\ 0 & t > t_0 \end{cases} \quad (52)$$

In the above equations,  $A_2$  is the heat pulse amplitude, defined as

$$A_2 = \sigma(T_b^4 - T_0^4) \quad (53)$$

where  $T_b$  and  $T_0$  are, respectively, the given boundary temperature  $T_b = 305$  K and reference temperature  $T_0 = 300$  K.  $\sigma$  is the Stephen-Boltzmann constant. Since the ballistic thermal wave

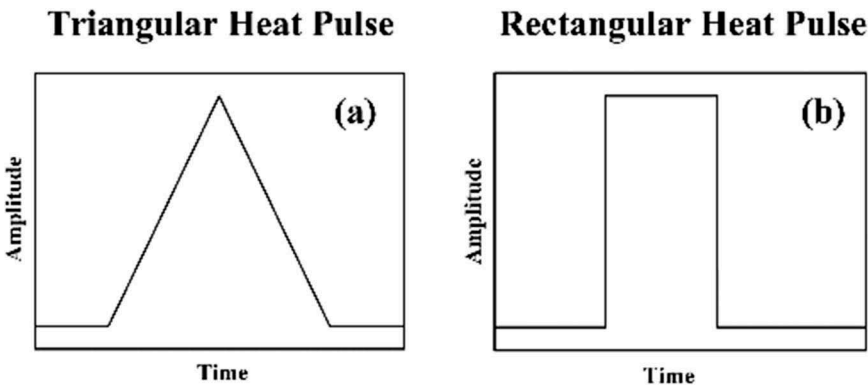
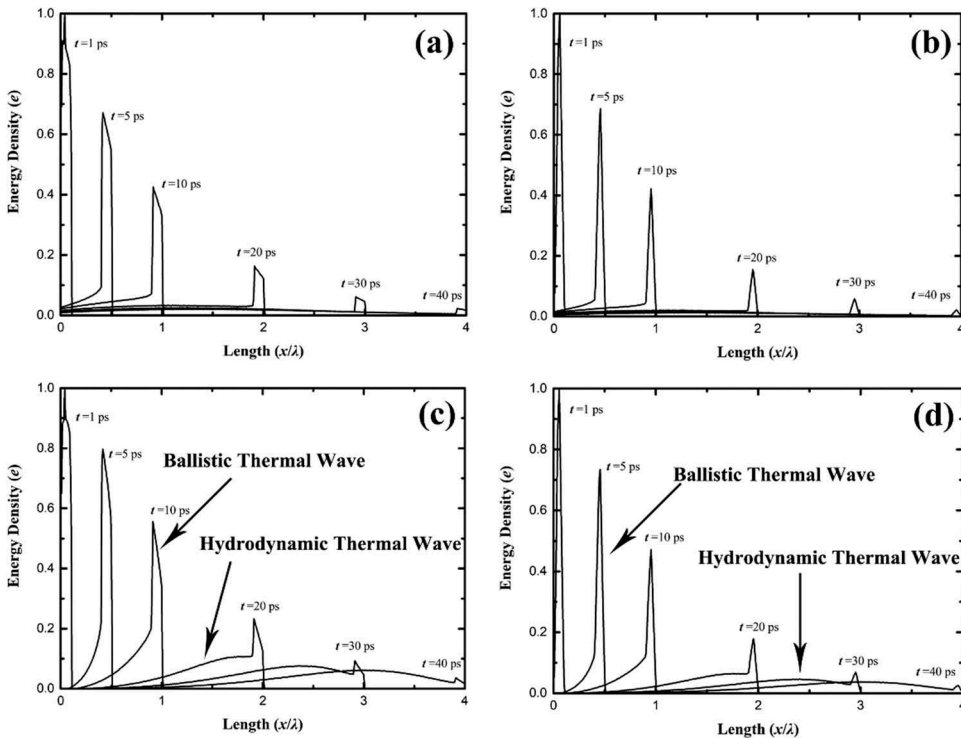


Figure 14. Shapes of the heat pulse applied to the left boundary.

dissipates exponentially with propagation distance, the profiles are displayed in the range from 0 to  $4\lambda$  before it is totally dissipated. The energy distribution patterns along with time of the ballistic thermal wave and hydrodynamic thermal wave have already been plotted in Figure 15. As for ballistic thermal wave, the mean-free path of R process is taken to be  $10\lambda$  and N process is ignored. For hydrodynamic thermal wave, phonon collisions are significant and N process dominates the whole scattering process while R process is ignored.

The behaviors of ballistic thermal wave have been investigated by Tang et al. [40–43]. It has been found that since the phonons are almost free from scatterings, the propagation behaviors of ballistic thermal wave are significantly influenced by the boundary conditions. And the directional emission has higher indexes of the energy MSD-time than Lambert emission, because the Lambert emission boundary introduces more spatial dispersion of phonons [42]. Meanwhile, the speed of the ballistic thermal wave is demonstrated to be the phonon group velocity. Here, in this model, only the ballistic thermal waves produced by directional emission boundary are considered. Therefore, the spatial dispersion can be ignored, and the behaviors are influenced only by R process, whose influence is called resistance dissipation in this paper. Compared with resistance dissipation, the influence on the wave profiles by spatial dispersive phonon distribution is called the spatial dissipation. The characteristics of ballistic thermal wave which is only influenced by resistance dissipation can be found from Figure 15a,b. First, the propagation distance is limited to one or two MFP because the profiles dissipate exponentially. Second, the propagation speed of ballistic thermal wave is the phonon group velocity as it has been demonstrated in the reference [43]. When the phonon branches and dispersion relation are considered, the speed of wave front is determined by the highest speed of phonons. Third, the shapes of the distribution profiles are maintained during propagation. When the



**Figure 15.** Propagation patterns of the energy density distribution for the ballistic thermal wave and hydrodynamic thermal wave under heat flux boundary condition. (a) and (b) are the energy density patterns of ballistic thermal wave where N process is ignored with a rectangular heat pulse (a) and a triangular heat pulse (b). (c) and (d) are the patterns of hydrodynamic thermal wave where R process is ignored with a rectangular heat pulse (c) and a triangular heat pulse (d).

inputting heat pulse is rectangular, the thermal wave has a trapezoid shape until ballistic phonons are totally scattered. It is the same for triangular heat pulse, as shown in Figure 15a,b. Thus, the ways of heating are important. Finally, the resistance dissipation destroys the drift behaviors of phonons and leaves a diffusive energy distribution after the thermal waves pass through. Therefore, the energy density behind the wave peak won't be zero and a temperature rise can be found. Meanwhile, when temperature boundary is applied, the boundary emission follows Lambert distribution and the spatial dissipation also takes effect in ballistic thermal waves.

Hydrodynamic thermal waves, which are free from resistance dissipation and influenced only by spatial dissipation, are plotted in Figure 15c,d. The sharp front represents the ballistic thermal wave because these phonons are not scattered and the hydrodynamic thermal wave is behind it, as shown in the figure. They enjoy longer travel distance than ballistic thermal waves. Due to the conservation of phonon momentum, the propagation distance can be up to 10 MFP. Second, although it was declared that the speed of thermal wave was supposed to be  $v_{sound}/\sqrt{3}$ , where  $v_{sound}$  is the speed of sound wave, it is found that the relationship might be not true. The definition of thermal wave speed is difficult because of the spatial dissipation and every part of the profile has different speed. The position of the wave front and that of the wave peak are plotted along with time as Figure 16. The wave front and wave peak propagate with constant speeds, but the ratio of them is 1.62, which is a little lower than  $\sqrt{3}$ , implying a higher peak speed than the prediction. The speed of wave peak represents the speed of maximum energy density, instead of the speed of thermal waves. Third, the final profile patterns get to be the same as time goes on. These shapes are free from the ways of heating, because when all the phonons are scattered, they follow the same distribution, namely the displaced Plank distribution. Finally, since all the phonon momentum is conserved, no thermal energy is left behind the waves. Thus, all the phonons keep moving forward, even though their speed might be slow. Another difference that can be told from Figure 15c,d is that the ballistic thermal wave has a higher wave peak than the hydrodynamic thermal wave because the energy in ballistic thermal wave is more concentrated.

Spatial dissipation and resistance dissipation influence the thermal waves in different ways [41–43]. Spatial dissipation conserves the phonon momentum so that the heat flux is conserved while the

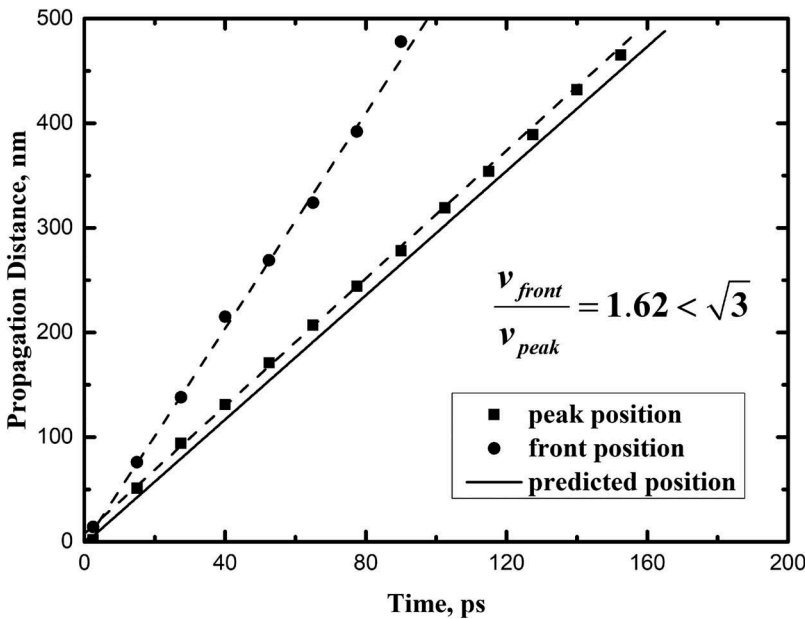


Figure 16. Positions of the wave peak and the wave front of the hydrodynamic thermal wave profiles along with the time.

distribution is dispersive. However, it makes the wavelength longer and peak value lower because of the speed difference of phonons. Resistance dissipation keeps the thermal wave shapes and decreases the peak value. At the same time, the heat flux is reduced.

### 3.2.2. Hyperbolic models

Since the propagation patterns of thermal wave are mainly influenced by resistance dissipation and spatial dissipation, macroscopic heat conduction equations are supposed to include these two effects. In Cattaneo-Vernotte equation [27,28],

$$\mathbf{q} + \tau \frac{\partial \mathbf{q}}{\partial t} = -k \nabla T \quad (54)$$

the first term depicts the resistance dissipation well and it gives an exponential dissipation figure. However, the spatial dissipation is not considered in this equation. Guyer-Krumhansl equation [31,32] attempts to include the spatial dissipation by adding a gradient term of the divergence of heat flux,

$$\mathbf{q} + \tau_R \frac{\partial \mathbf{q}}{\partial t} = -k \nabla T + \frac{\tau_R \tau_N v_s^2}{5} (\nabla^2 \mathbf{q} + 2 \nabla \nabla \cdot \mathbf{q}) \quad (55)$$

Nevertheless, it transforms the hyperbolic heat conduction equation into a parabolic one, leading to other problems. In one-dimensional heat conduction problem, Equation (56) becomes

$$q + \tau_R \frac{\partial q}{\partial t} = -k \frac{\partial T}{\partial x} + \frac{3 \tau_R \tau_N v_s^2}{5} \frac{\partial^2 q}{\partial x^2} \quad (56)$$

The last term in the above equation can be regarded as the viscous term of heat flux, analogous with Navier-Stokes equation in fluid mechanics. As it is known, the first term, which represents the resistance dissipation, leads the profiles to dissipate exponentially. Therefore, here the first term is omitted so that the attention can be focused on the viscous effects,

$$\tau_R \frac{\partial q}{\partial t} = -k \frac{\partial T}{\partial x} + m \frac{\partial^2 q}{\partial x^2} \quad (57)$$

Another hydrodynamic model is the thermomass (TM) model [34–36], which considers the propagation of extra mass due to thermal vibration. This model introduces the convective term, which represents the momentum drift,

$$\frac{\partial q_i}{\partial t} + \frac{\partial (\frac{q_i q_j}{e})}{\partial x_j} = -\frac{2 \gamma e}{c^2 \rho} \frac{\partial e}{\partial x_i} - \frac{2 \gamma e C_V}{K c^2} q_i \quad (58)$$

The second term is the convective term. To highlight the influences of phonon momentum drift, this equation in one-dimensional heat conduction problems is simplified to

$$\tau_{TM} \frac{\partial q}{\partial t} + \tau_{TM} \frac{\partial (\frac{q q}{e})}{\partial x} = -k \frac{\partial e}{\partial x} - q \quad (59)$$

And the last term is ignored for the same purpose,

$$\tau_{TM} \frac{\partial q}{\partial t} + \tau_{TM} \frac{\partial (\frac{q q}{e})}{\partial x} = -k \frac{\partial e}{\partial x} \quad (60)$$

As the MC method simulates a boundary value problem, where heat flux at the boundary is set to be

$$q(t, x = 0) = \begin{cases} q_0 & t \leq t_{pulse} \\ 0 & t > t_{pulse} \end{cases} \quad (61)$$

The initial conditions are

$$q(x, t = 0) = 0 \quad (62)$$

$$T(x, t = 0) = T_0 \quad (63)$$

In the numerical simulations, all the quantities are normalized and the heat pulse interval  $t_{pulse}$  is set to be 0.1. If there are no specific illustrations, the nondimensional coefficients are all set to be 1. The length of the regime is 10, which is normalized by MFP  $\lambda$ . The staggered grid is adopted where the temperature field and heat flux field are positioned at the nodes and between the nodes. As for the temporal term, forward difference algorithm is used and the spatial term is solved by the first-order upwind scheme. The grid number is set to be 1000 and the time interval is  $1 \times 10^{-6}$ . The simulation model is the same to Figure 12. More numerical details can be found in reference [68].

The simulation results depict the temperature distribution along with time for Equations (57) and (60) at  $t = 0.1, 0.3, 0.5, 0.7,$  and  $0.9$ . The effects of the viscous term have been shown in Figure 17a, where the profiles have longer wavelength and lower peak temperature with time going on. This tendency is much similar to that in the MC simulations. However, the differences are that the viscous term predicted a higher speed for the wave front and the viscosity adds to the dissipation, leaving the temperature rise behind the wave. In Figure 17b the convective term is found to establish a sharp wave front and make the thermal energy more concentrated. This pattern is different from the propagation patterns obtained from MC simulations with directional emission boundary.

These two models are not suitable to describe the spatial resistance, because neither of them consider the phonon velocity dispersion. If the influences of phonon bunches and dispersion relation are taken into consideration, the heat transport phenomena will become more complex. It requires further investigations to find a proper macroscale equation.

### 3.3. Resistance dissipation and Ziman hydrodynamics

When the influences of R process cannot be ignored and N process still dominates, the heat transport mode belongs to Ziman hydrodynamics [45]. Here, the spatial dissipation and resistance dissipation are both significant. At that time, both ballistic thermal wave and hydrodynamic thermal wave can be observed. When R process dominates the scattering process which means that the MFP

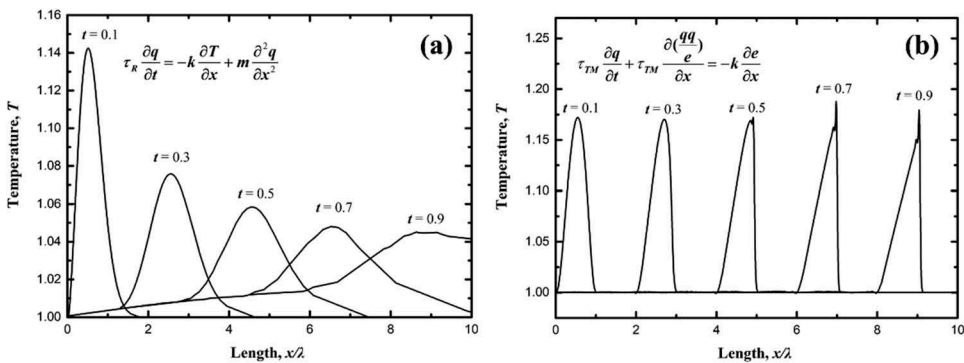
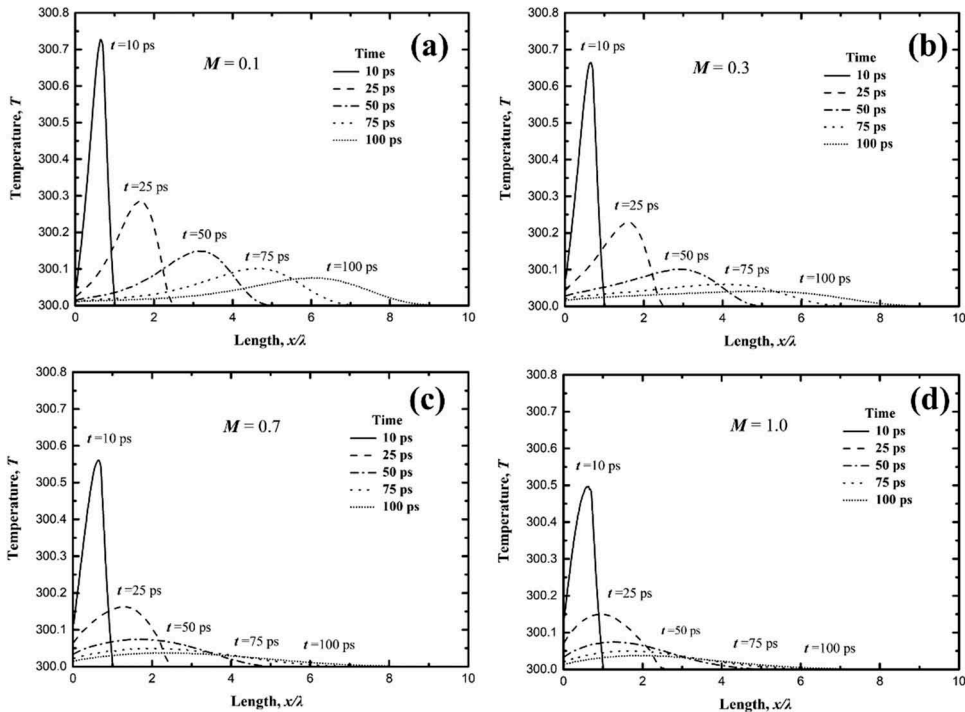


Figure 17. Temperature distribution patterns along with time predicted by simplified GK equation and TM equation in one-dimensional heat conduction problems.

of resistance scattering process is shorter than that of normal scattering process, thermal waves dissipate rapidly before enough phonons are scattered by N process. And it is difficult to observe the hydrodynamic thermal wave. The scattering probability  $M$  (Equation (14)) is adopted to represent the portion of R process in the total scattering rate. When  $M > 0.5$ , R process is stronger than N process and vice versa. At the left limit when  $M = 0$ , the heat transport mode belongs to Poiseuille hydrodynamics. When  $M > 0$  and  $M < 0.5$ , it is the Ziman hydrodynamics. When  $M > 0.5$ , the diffusive effect governs. And at the right limit  $M = 1.0$ , the thermal energy transport process can be described by Fourier's law, where only the resistance dissipation is considered.

Here in this section, the propagation characteristics of thermal wave in the Ziman hydrodynamic regime and the diffusive regime are discussed. Figure 18 shows the temperature distribution profile of thermal wave along with time at different values of  $M$ . The thermal wave is induced by the left temperature boundary  $T = 301$  K and the reference temperature is 300 K. The schematic diagram is the same to Figure 12. It can be found that there is no obvious boundary between Ziman hydrodynamic regime and diffusive regime, so the transition is smooth. In Figure 18a, the temperature profile spreads forward when the thermal energy propagates from the left boundary to the right. Compared with the thermal wave in Poiseuille hydrodynamic regime, both of their wave peaks have the tendency to move forward and Figure 18a displays stronger dissipation effect, which comes from resistance dissipation. When  $M = 0.3$  in Figure 18b, the moving tendency of wave peak is obvious at the beginning and diminishes at last. However, it does not mean that the thermal energy stops propagating. It continues spreading forward, as the local energy density gradient determines the heat flux. The behaviors of wave peak imply the exhaustion of initial phonon momentum. When  $M = 0.7$  in Figure 18c, which is already in the diffusive regime according to the definition, it is hard to tell the movement of thermal wave. The thermal energy cannot flow from the low temperature to the high temperature, because here the diffusive equation governs. When  $M = 1.0$  in Figure 18d, it can be predicted by Fourier's law.



**Figure 18.** Comparisons of the temperature distribution patterns along with time at different scattering probability values,  $M = 0.1$  (a), 0.3 (b), 0.7 (c) and 1.0 (d).

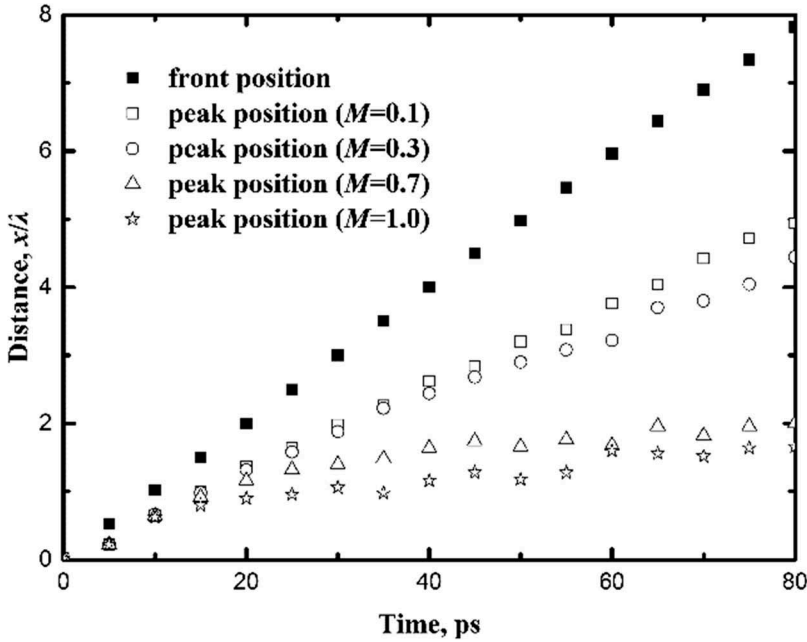


**Figure 19.** Positions of the wave front and wave peak of thermal waves in the media along with time at  $M = 0.1, 0.3, 0.7,$  and  $1.0$ .

Figure 19 shows the position figures of wave front and wave peak of thermal wave at different  $M$ , and the line slope implies the wave speed. As the speed of wave front equals the speed of ballistic thermal wave, they are the same at different values of  $M$ . What is concerned here is the speed of the wave peak. They are almost the same when the traveling distance is smaller than one MFP  $\lambda$ . When the traveling distance is longer than  $\lambda$ , the peak position continues moving forward and the speed slows down then. With larger  $M$ , the speed becomes slower. When the scattering probability  $M$  is larger than  $0.5$ , the speed of wave peak decreases to zero when time  $t$  is larger than  $20$  ps. The differences of speeds demonstrate the transition of transport mode from hydrodynamic regime to diffusive regime. Since the phonon momentum is conserved, phonon density profiles in Poiseuille hydrodynamic regime propagate with a constant speed. When R process takes effects, the moving tendency decreases with phonon momentum destruction. In the diffusive regime, there are no obvious transport phenomena of thermal energy profiles. Thus, the speed becomes zero.

#### 4. Conclusions

This paper intends to give a relatively microscopic description for thermal waves in phonon hydrodynamic regime based on an improved phonon MC algorithm. The MC algorithm is developed based on the Callaway's dual relaxation time model. In this model, phonon scatterings are divided into two types, namely normal scattering process and resistance scattering process. The behaviors of phonons after N process are determined by the local energy density and phonon momentum. As it is demonstrated that phonons in different frequencies in phonon hydrodynamics share the same drift velocity, the phonon momentum can be represented by the phonon drift velocity. The application of control-variate variance-reduction method in the MC algorithm leads to the problem of negative probability, resulting in the mathematical dissipation. Positive and negative energy particle couplings are adopted to deal with this problem, and make sure the phonon momentum is conserved under the condition of thermal energy conservation. Besides, this algorithm is based on more general three-dimensional regime, and it has various applications. Furthermore, by

introducing the concept of scattering probability  $M$ , it can be used to deal with the coupling of N process and R process in heat conduction.

The wavelike behaviors of heat transport have been demonstrated in Poiseuille hydrodynamic regime from the view of phonons. Overshooting and diffraction phenomena have been observed. One problem that should be noticed is the definition of temperature, which is not suitable for transient heat transport. In this paper, the temperature is more like the symbol of local energy density. The overshooting phenomenon occurs when thermal wave is reflected back by the boundary or two thermal waves meet with each other. It is demonstrated that superposition principle takes effect and a higher temperature peak shows up. Another wave characteristic is the diffraction, which occurs when the waves get across the obstacles or holes with the size equivalent to or smaller than the wavelength. When thermal waves go across a hole, new waves are found to spread away with the hole as new wave source.

One advantage of the MC method is that it deals with N process and R process individually and it is easy to analyze the influences of each process. According to the differences in phonon scatterings, the thermal waves are divided into two categories, namely ballistic thermal wave and hydrodynamic thermal wave. They are sorted by the scattering type, traveling length, speed, and shapes. The concept of second sound is thought to be the experimental observation of the combination of these two kinds of waves. When thermal wave propagates, two kinds of dissipation are involved, that is, spatial dissipation and resistance dissipation. The former keeps the conservation of phonon momentum, but lengthens the wavelength and decreases the peak value, while the latter reduces the phonon momentum and maintains the wavelength. Besides, the temperature profiles predicted by the phonon MC simulations are compared with those hyperbolic heat conduction equations. The influences of viscous term and convective term are revealed by numerical simulations. It is found that the current models are not suitable to describe the spatial dissipation effect, which results from the spatial dispersion of phonon directions. More accurate hyperbolic models are required in further investigation.

When resistance scattering process cannot be ignored, the heat transport mode belongs to Ziman hydrodynamic regime or diffusive regimes. These two heat conduction modes are different in propagation distances, propagation speeds and patterns. As the scattering probability  $M$  increases from 0 to 1, the propagation patterns of thermal wave go from hyperbolic type to parabolic type, and the energy transport efficiency becomes lower and lower.

Here, the influences of dispersion relation, phonon branches, and the difference of density of state are omitted to make a simple model. However, they are important in actual materials and might give different predictions on thermal waves. Therefore, this paper avoids the quantitative description and tries to give the qualitative principles and theoretical explanations. Though this paper aims to reveal the intrinsic nature of different types of thermal waves, further investigations are highly desired.

## Declaration of interest statement

The authors declared that they had no interest conflict.

## Funding

This work was financially supported by the National Natural Science Foundation of China [Grant No. 51825601, 51676108].

## References

- [1] D. D. Joseph and L. Preziosi, "Heat waves," *Rev. Mod. Phys.*, vol. 61, no. 1, pp. 41–73, 1989. DOI: [10.1103/RevModPhys.61.41](https://doi.org/10.1103/RevModPhys.61.41).

- [2] B. Straughan, *Heat Waves*. Springer Science & Business Media, New York, 2011.
- [3] M. Ozisik and D. Tzou, "On the wave theory in heat conduction," *J. Heat Transfer*, vol. 116, no. 3, pp. 526–535, 1994. DOI: [10.1115/1.2910903](https://doi.org/10.1115/1.2910903).
- [4] T. Shimazaki, M. Murakami, and T. Iida, "Second sound wave heat transfer, thermal boundary layer formation and boiling: Highly transient heat transport phenomena in He II," *Cryogenics*, vol. 35, no. 10, pp. 645–651, 1995. DOI: [10.1016/S0011-2275\(99\)80005-8](https://doi.org/10.1016/S0011-2275(99)80005-8).
- [5] J. P. Chu and W. Hsin-Sen, "Propagation and reflection of thermal waves in a rectangular plate," *Numer. Heat Transfer Part A: Appl.*, vol. 36, no. 1, pp. 51–74, 1999. DOI: [10.1080/104077899274895](https://doi.org/10.1080/104077899274895).
- [6] W. B. Lor and H. S. Chu, "Propagation of thermal waves in a composite medium with interface thermal boundary resistance," *Numer. Heat Transfer Part A: Appl.*, vol. 36, no. 7, pp. 681–697, 1999. DOI: [10.1080/104077899274516](https://doi.org/10.1080/104077899274516).
- [7] W. B. Lor and H. S. Chu, "Effect of interface thermal resistance on heat transfer in a composite medium using the thermal wave model," *Int. J. Heat Mass Transf.*, vol. 43, no. 5, pp. 653–663, 2000. DOI: [10.1016/S0017-9310\(99\)00178-7](https://doi.org/10.1016/S0017-9310(99)00178-7).
- [8] B. Shen and P. Zhang, "Notable physical anomalies manifested in non-Fourier heat conduction under the dual-phase-lag model," *Int. J. Heat Mass Transf.*, vol. 51, no. 7–8, pp. 1713–1727, 2008. DOI: [10.1016/j.ijheatmasstransfer.2007.07.039](https://doi.org/10.1016/j.ijheatmasstransfer.2007.07.039).
- [9] M. Al-Nimr, M. Naji, and S. Al-Wardat, "Overshooting phenomenon in the hyperbolic heat conduction model," *Jpn. J. Appl. Phys.*, vol. 42, no. 8R, pp. 5383, 2003. DOI: [10.1143/JJAP.42.5383](https://doi.org/10.1143/JJAP.42.5383).
- [10] M. Xu, J. Guo, L. Wang, and L. Cheng, "Thermal wave interference as the origin of the overshooting phenomenon in dual-phase-lagging heat conduction," *Int. J. Therm. Sci.*, vol. 50, no. 5, pp. 825–830, 2011. DOI: [10.1016/j.ijthermalsci.2010.12.006](https://doi.org/10.1016/j.ijthermalsci.2010.12.006).
- [11] M. Özişik and B. Vick, "Propagation and reflection of thermal waves in a finite medium," *Int. J. Heat Mass Transf.*, vol. 27, no. 10, pp. 1845–1854, 1984. DOI: [10.1016/0017-9310\(84\)90166-2](https://doi.org/10.1016/0017-9310(84)90166-2).
- [12] D. Y. Tzou, "Reflection and refraction of thermal waves from a surface or an interface between dissimilar materials," *Int. J. Heat Mass Transf.*, vol. 36, no. 2, pp. 401–410, 1993. DOI: [10.1016/0017-9310\(93\)80016-N](https://doi.org/10.1016/0017-9310(93)80016-N).
- [13] B. D. Nie and B. Y. Cao, "Reflection and refraction of a thermal wave at an ideal interface," *Int. J. Heat Mass Transf.*, vol. 116, pp. 314–328, 2018. DOI: [10.1016/j.ijheatmasstransfer.2017.09.043](https://doi.org/10.1016/j.ijheatmasstransfer.2017.09.043).
- [14] J. C. Maxwell, "IV. On the dynamical theory of gases," *Philos. Trans. R. Soc. London*, vol. 157, pp. 49–88, 1867.
- [15] W. Nernst, *Die theoretischen und experimentellen Grundlagen des neuen Wärmesatzes*, Knapp, Halle, 1917.
- [16] L. Onsager, "Reciprocal relations in irreversible processes. II," *Phys. Rev.*, vol. 38, no. 12, pp. 2265–2279, 1931. DOI: [10.1103/PhysRev.38.2265](https://doi.org/10.1103/PhysRev.38.2265).
- [17] S. N. Li and B. Y. Cao, "Anomalous heat diffusion from fractional Fokker-Planck equation," *Appl. Math. Lett.*, vol. 99, pp. 105992, 2020. DOI: [10.1016/j.aml.2019.07.023](https://doi.org/10.1016/j.aml.2019.07.023).
- [18] Y. C. Hua, H. L. Li, and B. Y. Cao, "Thermal spreading resistance in ballistic-diffusive regime in GaN HEMTs," *IEEE Trans. Electron. Devices*, vol. 66, no. 8, pp. 3296–3301, 2019. DOI: [10.1109/TED.2019.2922221](https://doi.org/10.1109/TED.2019.2922221).
- [19] L. Tisza, "Sur la Supraconductibilit e thermique de l'helium II liquide et la statistique de Bose-Einstein," *CR Acad. Sci.*, vol. 207, pp. 1035, 1938.
- [20] L. Landau, "Theory of the superfluidity of helium II," *Phys. Rev.*, vol. 60, no. 4, pp. 356–358, 1941. DOI: [10.1103/PhysRev.60.356](https://doi.org/10.1103/PhysRev.60.356).
- [21] V. Peshkov, "Second sound in helium," *J. Phys.*, vol. 8, no. 1-6, pp. 381, 1944.
- [22] M. Chester, "Second sound in solids," *Phys. Rev.*, vol. 131, no. 5, pp. 2013–2015, 1963. DOI: [10.1103/PhysRev.131.2013](https://doi.org/10.1103/PhysRev.131.2013).
- [23] C. C. Ackerman, B. Bertman, H. A. Fairbank, and R. A. Guyer, "Second sound in solid helium," *Phys. Rev. Lett.*, vol. 16, no. 18, pp. 789–791, 1966. DOI: [10.1103/PhysRevLett.16.789](https://doi.org/10.1103/PhysRevLett.16.789).
- [24] T. McNelly, *et al.* "Heat pulses in NaF: Onset of second sound," *Phys. Rev. Lett.*, vol. 24, no. 3, pp. 100, 1970. DOI: [10.1103/PhysRevLett.24.100](https://doi.org/10.1103/PhysRevLett.24.100).
- [25] H. E. Jackson, C. T. Walker, and T. F. McNelly, "Second sound in NaF," *Phys. Rev. Lett.*, vol. 25, no. 1, pp. 26, 1970. DOI: [10.1103/PhysRevLett.25.26](https://doi.org/10.1103/PhysRevLett.25.26).
- [26] V. Narayanamurti and R. Dynes, "Observation of second sound in bismuth," *Phys. Rev. Lett.*, vol. 28, no. 22, pp. 1461, 1972. DOI: [10.1103/PhysRevLett.28.1461](https://doi.org/10.1103/PhysRevLett.28.1461).
- [27] C. Cattaneo, "Sulla conduzione del calore," *Atti. Sem. Mat. Fis. Univ. Modena*, vol. 3, pp. 83–101, 1948.
- [28] P. Vernotte, "Paradoxes in the continuous theory of the heat equation," *CR Acad. Sci.*, vol. 246, pp. 154–3, 1958.
- [29] D. Y. Tzou, "The generalized lagging response in small-scale and high-rate heating," *Int. J. Heat Mass Transf.*, vol. 38, no. 17, pp. 3231–3240, 1995. DOI: [10.1016/0017-9310\(95\)00052-B](https://doi.org/10.1016/0017-9310(95)00052-B).
- [30] D. Y. Tzou, "Experimental support for the lagging behavior in heat propagation," *J. Thermophys. Heat Transfer*, vol. 9, no. 4, pp. 686–693, 1995. DOI: [10.2514/3.725](https://doi.org/10.2514/3.725).
- [31] R. A. Guyer and J. A. Krumhansl, "Solution of the linearized phonon Boltzmann equation," *Phys. Rev.*, vol. 148, no. 2, pp. 766–778, 1966. DOI: [10.1103/PhysRev.148.766](https://doi.org/10.1103/PhysRev.148.766).
- [32] R. A. Guyer and J. A. Krumhansl, "Thermal conductivity, second sound, and phonon hydrodynamic phenomena in nonmetallic crystals," *Phys. Rev.*, vol. 148, no. 2, pp. 778–788, 1966. DOI: [10.1103/PhysRev.148.778](https://doi.org/10.1103/PhysRev.148.778).

- [33] M. E. Gurtin and A. C. Pipkin, "A general theory of heat conduction with finite wave speeds," *Arch. Ration. Mech. Anal.*, vol. 31, no. 2, pp. 113–126, 1968. DOI: [10.1007/BF00281373](https://doi.org/10.1007/BF00281373).
- [34] B. Y. Cao and Z. Y. Guo, "Equation of motion of a phonon gas and non-Fourier heat conduction," *J. Appl. Phys.*, vol. 102, no. 5, pp. 053503, 2007. DOI: [10.1063/1.2775215](https://doi.org/10.1063/1.2775215).
- [35] B. Y. Cao, Y. Dong, and Z. Y. Guo, "Generalized heat conduction laws based on thermomass theory and phonon hydrodynamics," *J. Appl. Phys.*, vol. 110, no. 6, pp. 063504, 2011. DOI: [10.1063/1.3634113](https://doi.org/10.1063/1.3634113).
- [36] Z. Y. Guo, "Energy-mass duality of heat and its applications," *ES Energy Environ.*, vol. 1, pp. 4–15, 2018.
- [37] G. Chen, "Ballistic-diffusive equations for transient heat conduction from nano to macroscales," *J. Heat Transfer*, vol. 124, no. 2, pp. 320–328, 2002. DOI: [10.1115/1.1447938](https://doi.org/10.1115/1.1447938).
- [38] Y. C. Hua, Y. Dong, and B. Y. Cao, "Monte Carlo simulation of phonon ballistic diffusive heat conduction in silicon nanofilm," *Acta Physica Sinica*, vol. 78, pp. 755–759, 2013.
- [39] Y. C. Hua and B. Y. Cao, "Phonon ballistic-diffusive heat conduction in silicon nanofilms by Monte Carlo simulations," *Int. J. Heat Mass Transf.*, vol. 78, pp. 755–759, 2014. DOI: [10.1016/j.ijheatmasstransfer.2014.07.037](https://doi.org/10.1016/j.ijheatmasstransfer.2014.07.037).
- [40] D. S. Tang, Y. C. Hua, B. D. Nie, and B. Y. Cao, "Phonon wave propagation in ballistic-diffusive regime," *J. Appl. Phys.*, vol. 119, pp. 124301, 2016.
- [41] D. S. Tang and B. Y. Cao, "Ballistic thermal wave propagation along nanowires modeled using phonon Monte Carlo simulations," *Appl. Therm. Eng.*, vol. 117, pp. 609–616, 2017. DOI: [10.1016/j.applthermaleng.2017.02.078](https://doi.org/10.1016/j.applthermaleng.2017.02.078).
- [42] B. Y. Cao and D. S. Tang, "Superballistic characteristics in transient phonon ballistic-diffusive transport," *Appl. Phys. Lett.*, vol. 111, no. 11, pp. 113109, 2017. DOI: [10.1063/1.5003639](https://doi.org/10.1063/1.5003639).
- [43] D. S. Tang, Y. C. Hua, and B. Y. Cao, "Thermal wave propagation through nanofilms in ballistic-diffusive regime by Monte Carlo simulations," *Int. J. Therm. Sci.*, vol. 109, pp. 81–89, 2016. DOI: [10.1016/j.ijthermalsci.2016.05.030](https://doi.org/10.1016/j.ijthermalsci.2016.05.030).
- [44] S. Lee, D. Broido, K. Esfarjani, and G. Chen, "Hydrodynamic phonon transport in suspended graphene," *Nat. Commun.*, vol. 6, pp. 6290, Feb. 18 2015. DOI: [10.1038/ncomms7290](https://doi.org/10.1038/ncomms7290).
- [45] A. Cepellotti, *et al.*, "Phonon hydrodynamics in two-dimensional materials," *Nat. Commun.*, vol. 6, no. 1, pp. 6400, Mar. 6 2015. DOI: [10.1038/ncomms7400](https://doi.org/10.1038/ncomms7400).
- [46] B. N. Narozhny, I. V. Gornyi, M. Titov, M. Schütt, and A. D. Mirlin, "Hydrodynamics in graphene: Linear-response transport," *Phys. Rev. B*, vol. 91, no. 3, 2015. DOI: [10.1103/PhysRevB.91.035414](https://doi.org/10.1103/PhysRevB.91.035414).
- [47] Y. Guo and M. Wang, "Phonon hydrodynamics and its applications in nanoscale heat transport," *Phys. Rep.*, vol. 595, pp. 1–44, 2015. DOI: [10.1016/j.physrep.2015.07.003](https://doi.org/10.1016/j.physrep.2015.07.003).
- [48] S. Lee and L. Lindsay, "Hydrodynamic phonon drift and second sound in a (20,20) single-wall carbon nanotube," *Phys. Rev. B*, vol. 95, no. 18, 2017. DOI: [10.1103/PhysRevB.95.184304](https://doi.org/10.1103/PhysRevB.95.184304).
- [49] X. Li and S. Lee, "Role of hydrodynamic viscosity on phonon transport in suspended graphene," *Phys. Rev. B*, vol. 97, no. 9, pp. 094309, 2018. DOI: [10.1103/PhysRevB.97.094309](https://doi.org/10.1103/PhysRevB.97.094309).
- [50] X. Li and S. Lee, "Crossover of ballistic, hydrodynamic, and diffusive phonon transport in suspended graphene," *Phys. Rev. B*, vol. 99, no. 8, pp. 085202, 2019. DOI: [10.1103/PhysRevB.99.085202](https://doi.org/10.1103/PhysRevB.99.085202).
- [51] X. L. Sangyeop Lee, "Hydrodynamic Phonon Transport Past, Present, and Prospect". preprint arXiv:1903.05731 [□2019](https://arxiv.org/abs/1903.05731).
- [52] S. Huberman, *et al.* "Observation of second sound in graphite at temperatures above 100 K," *Science*, vol. 364, no. 6438, pp. 375–379, 2019. DOI: [10.1126/science.aav3548](https://doi.org/10.1126/science.aav3548).
- [53] W. J. Yao and B. Y. Cao, "Thermal wave propagation in graphene studied by molecular dynamics simulations," *Chin. Sci. Bull.*, vol. 59, no. 27, pp. 3495–3503, 2014. DOI: [10.1007/s11434-014-0472-6](https://doi.org/10.1007/s11434-014-0472-6).
- [54] D. Lacroix, K. Joulain, and D. Lemonnier, "Monte Carlo transient phonon transport in silicon and germanium at nanoscales," *Phys. Rev. B*, vol. 72, no. 6, 2005. DOI: [10.1103/PhysRevB.72.064305](https://doi.org/10.1103/PhysRevB.72.064305).
- [55] M. S. Jeng, R. Yang, D. Song, and G. Chen, "Modeling the thermal conductivity and phonon transport in nanoparticle composites using Monte Carlo simulation," *J. Heat Transfer*, vol. 130, no. 4, pp. 042410, 2008. DOI: [10.1115/1.2818765](https://doi.org/10.1115/1.2818765).
- [56] Y. Chen, D. Li, J. R. Lukes, and A. Majumdar, "Monte Carlo simulation of silicon nanowire thermal conductivity," *J. Heat Transfer*, vol. 127, no. 10, pp. 1129–1137, 2005. DOI: [10.1115/1.2035114](https://doi.org/10.1115/1.2035114).
- [57] Q. Hao, G. Chen, and M. S. Jeng, "Frequency-dependent Monte Carlo simulations of phonon transport in two-dimensional porous silicon with aligned pores," *J. Appl. Phys.*, vol. 106, no. 11, pp.114321, 2009. DOI: [10.1063/1.3266169](https://doi.org/10.1063/1.3266169).
- [58] S. Mazumder and A. Majumdar, "Monte Carlo study of phonon transport in solid thin films including dispersion and polarization," *J. Heat Transfer*, vol. 123, no. 4, pp. 749–759, 2001. DOI: [10.1115/1.1377018](https://doi.org/10.1115/1.1377018).
- [59] J. P. M. Péraud and N. G. Hadjiconstantinou, "Efficient simulation of multidimensional phonon transport using energy-based variance-reduced Monte Carlo formulations," *Phys. Rev. B*, vol. 84, no. 20, 2011. DOI: [10.1103/PhysRevB.84.205331](https://doi.org/10.1103/PhysRevB.84.205331).
- [60] H. McGaughey and A. Jain, "Nanostructure thermal conductivity prediction by Monte Carlo sampling of phonon free paths," *Appl. Phys. Lett.*, vol. 100, no. 6, pp.061911, 2012. DOI: [10.1063/1.3683539](https://doi.org/10.1063/1.3683539).

- [61] J. P. M. Péraud, C. D. Landon, and N. G. Hadjiconstantinou, “Monte Carlo methods for solving the Boltzmann transport equation,” *Annu. Rev. Heat Transfer*, vol. 17, pp. 205–265, 2014. DOI: [10.1615/AnnualRevHeatTransfer.2014007381](https://doi.org/10.1615/AnnualRevHeatTransfer.2014007381).
- [62] L. Ma, R. Mei, X. Zhao, and H. Sun, “Monte Carlo simulation of single-crystalline PbSe nanowire thermal conductivity using first-principle phonon properties,” *Semicond. Sci. Technol.*, vol. 32, no. 9, pp.095008, 2017. DOI: [10.1088/1361-6641/aa7c15](https://doi.org/10.1088/1361-6641/aa7c15).
- [63] S. Lee, X. Li, and R. Guo, “Thermal resistance by transition between collective and non-collective phonon flows in graphitic materials,” *Nanoscale Microscale Thermophys. Eng.*, vol. 23, no. 3, pp. 247–258, 2019. DOI: [10.1080/15567265.2019.1575497](https://doi.org/10.1080/15567265.2019.1575497).
- [64] L. Lindsay, C. Hua, X. L. Ruan, and S. Lee, “Survey of ab initio phonon thermal transport,” *Mater. Today Phys.*, vol. 7, pp. 106–120, 2018. DOI: [10.1016/j.mtphys.2018.11.008](https://doi.org/10.1016/j.mtphys.2018.11.008).
- [65] J. Callaway, “Model for Lattice Thermal Conductivity at Low Temperatures,” *Phys. Rev.*, vol. 113, no. 4, pp. 1046–1051, 1959. DOI: [10.1103/PhysRev.113.1046](https://doi.org/10.1103/PhysRev.113.1046).
- [66] Y. Guo and M. Wang, “Heat transport in two-dimensional materials by directly solving the phonon Boltzmann equation under Callaway’s dual relaxation model,” *Phys. Rev. B*, vol. 96, no. 13, 2017. DOI: [10.1103/PhysRevB.96.134312](https://doi.org/10.1103/PhysRevB.96.134312).
- [67] R. J. Hardy, “Phonon Boltzmann equation and second sound in solids,” *Phys. Rev. B*, vol. 2, no. 4, pp. 1193, 1970. DOI: [10.1103/PhysRevB.2.1193](https://doi.org/10.1103/PhysRevB.2.1193).
- [68] B. D. Nie and B. Y. Cao, “Three mathematical representations and an improved ADI method for hyperbolic heat conduction,” *Int. J. Heat Mass Transf.*, vol. 135, pp. 974–984, 2019. DOI: [10.1016/j.ijheatmasstransfer.2019.02.026](https://doi.org/10.1016/j.ijheatmasstransfer.2019.02.026).